Single-dose radiotherapy disables tumor cell homologous recombination via ischemia/reperfusion injury

Sahra Bodo,[1] Cécile Campagne,[1] Tin Htwe Thin,[1] Daniel S. Higginson,[1] H. Alberto Vargas,[2] Guoqiang Hua,[1] John D. Fuller,[3] Ellen Ackerstaff,[4] James Russell,[4] Zhigang Zhang,[5] Stefan Klingler,[3] HyungJoon Cho,[4] Matthew G. Kaag,[6] Yousef Mazaheri,[2] Andreas Rimner,[1] Katia Manova-Todorova,[7] Boris Epel,[8] Joan Zatcky,[1] Cristian R. Cleary,[1] Shyam S. Rao,[1] Yoshiya Yamada,[1] Michael J. Zelefsky,[1] Howard J. Halpern,[8] Jason A. Koutcher,[4] Carlos Cordon-Cardo,[9] Carlo Greco,[10] Adriana Haimovitz-Friedman,[1] Evis Sala,[2] Simon N. Powell,[1] Richard Kolesnick,[3] and Zvi Fuks[1,10]

[1]Department of Radiation Oncology, [2]Department of Radiology, [3]Laboratory of Signal Transduction, [4]Department of Medical Physics, [5]Department of Epidemiology and Biostatistics, [6]Department of Surgery, and [7]Laboratory of Molecular Cytology, Memorial Sloan Kettering Cancer Center, New York, New York, USA. [8]Department of Radiation and Cellular Oncology, Center for EPR Imaging In Vivo Physiology, The University of Chicago, Chicago, Illinois, USA. [9]Department of Pathology, Mount Sinai School of Medicine, New York, New York, USA. [10]Champalimaud Centre, Lisbon, Portugal.

Tumor cure with conventional fractionated radiotherapy is 65%, dependent on tumor cell–autonomous gradual buildup of DNA double-strand break (DSB) misrepair. Here we report that single-dose radiotherapy (SDRT), a disruptive technique that ablates more than 90% of human cancers, operates a distinct dual-target mechanism, linking acid sphingomyelinase–mediated (ASMase-mediated) microvascular perfusion defects to DNA unrepair in tumor cells to confer tumor cell lethality. ASMase-mediated microcirculatory vasoconstriction after SDRT conferred an ischemic stress response within parenchymal tumor cells, with ROS triggering the evolutionarily conserved SUMO stress response, specifically depleting chromatin-associated free SUMO3. Whereas SUMO3, but not SUMO2, was indispensable for homology-directed repair (HDR) of DSBs, HDR loss of function after SDRT yielded DSB unrepair, chromosomal aberrations, and tumor clonogen demise. Vasoconstriction blockade with the endothelin-1 inhibitor BQ-123, or ROS scavenging after SDRT using peroxiredoxin-6 overexpression or the SOD mimetic tempol, prevented chromatin SUMO3 depletion, HDR loss of function, and SDRT tumor ablation. We also provide evidence of mouse-to-human translation of this biology in a randomized clinical trial, showing that 24 Gy SDRT, but not 3×9 Gy fractionation, coupled early tumor ischemia/reperfusion to human cancer ablation. The SDRT biology provides opportunities for mechanism-based selective tumor radiosensitization via accessing of SDRT/ASMase signaling, as current studies indicate that this pathway is tractable to pharmacologic intervention.

Introduction

While tumor cure in patients with localized primary disease treated with conventional fractionated radiotherapy is approximately 65% (1), new image-guided radiotherapy that precisely targets tumors in 3D yields an unprecedented >90% tumor ablation with a single 24-Gy exposure, irrespective of human tumor type (2, 3). This new approach to treat tumors with ultra-high single-dose radiotherapy (SDRT) holds promise as a leap in

cancer treatment, consistently ablating tumors resistant to frac-tionated radiotherapy (4, 5).

Conventional fractionated radiotherapy employs wide normal-tissue safety margins to avoid missing of tumors, and repeated daily low-dose (1.8–2.5 Gy) exposures. A single exposure at this dose range, although noncurative, induces extensive DNA damage, including potentially lethal DNA double-strand breaks (DSBs) (6), resolved by an adaptive DNA damage response (DDR), which coordinates cell cycle arrest and DSB repair (7). A therapeutic ratio is predicated on slow-dividing tissues being more radioresistant than rapidly dividing tumor cells (8), with slow-dividing tissues accruing less DNA repair errors as treatment progresses. Tumor cure versus local failure ultimately reflects the extent of misre-paired DNA damage, with radioresistant tumors repairing damage faithfully, while radiosensitive tumors manifest error-prone DSB repair (6, 9), with residual misrepaired DSBs promoting genomic instability and lethal chromosomal aberrations in progeny (10). Mammalian DSB repair is accomplished by canonical nonhomol-ogous end joining (NHEJ) and homology-directed repair (HDR), which normally protect chromosome integrity, while alternative NHEJ (alt-EJ) is error-prone, yielding potentially lethal errors (11). The single-target model of tumor cure by fractionation pos-its that outcome depends exclusively on fidelity of tumor cell–

autonomous DNA damage repair, with damage to host-derived stroma being insignificant (12).

Consistent with this model, extensive literature reports a highly reproducible rank ordering of human tumor-ablative dose by tumor type (13). Meta-analysis of 62 studies reports that cumulative doses for 50% durable tumor control (TCD_{50}) display a broad 4-fold span from 21 Gy in Hodgkin's disease to 83 Gy for stage III–IV head and neck tumors (13). However, dose buildup required for $\geq TCD_{90}$ of human tumors is restricted by risk of collateral normal-tissue damage, limiting overall cure to 65% (1).

Whereas proficiency of recent image-guidance technology in online tumor targeting enables near elimination of normal-tissue safety margins, clinical dose escalation studies have established a TCD_{90} for SDRT in diverse human tumors (2, 3) that surprisingly reveals that SDRT cures all tumor types within the same tight dose range, irrespective of whether tumors are sensitive or resistant to classical fractionated radiotherapy (2, 3). This uniform response suggests that SDRT might engage a distinct biologic mechanism of tumor cure.

Consistent with this notion, our recent studies of SDRT mouse models provided an alternative to the single-target paradigm of tumor cure by radiation. Our data indicate that, beginning at approximately 10 Gy, SDRT operates a dual-target mechanism of tumor cure, linking tumor microvascular injury mediated by acid sphingomyelinase (ASMase)/ceramide-mediated tumor microvascular injury in parenchymal tumor cells to yield tumor cell demise (14). Tumors implanted in $asmase^{-/-}$ mice become radioresistant (14, 15), and adenoviral delivery of ASMase exclusively to dividing neoangiogenic endothelium restores SDRT-induced cure (16). While we originally deemed ASMase/ceramide–mediated endothelial apoptosis as linking SDRT-induced vascular injury to tumor cell demise (14, 17), experiments reported here, designed to explore the onset of vascular dysfunction, showed that rapid ceramide-mediated ischemia/reperfusion (I/R) injury preceding endothelial apoptosis dysregulates DDR via generation of toxic reactive oxygen species (ROS) in parenchymal tumor cells. Mechanistically, ROS trigger the evolutionarily conserved small ubiquitin modifier (SUMO) stress response (SSR) (18, 19), depleting unconjugated chromatin-associated SUMO3, a protein modifier specifically required for activation of multiple mediators of HDR, yielding global inactivation of homologous recombination to yield massive tumor clonogen lethality.

Results

SDRT induces rapid I/R injury. Whereas our published data indicate that microvascular endothelial apoptosis in murine tumor allografts begins at 1.5–2 hours after high SDRT (20) and peaks at 4–6 hours (14), we studied perfusion dynamics associated with this response. Initial screening quantified perfusion-dependent transcapillary flux of the bisbenzimide fluorochrome Hoechst 33342 into tumor interstitial space, as described previously (21). Hoechst 33342 was injected intravenously in tumor-bearing $asmase^{+/+}$ or $asmase^{-/-}$ littermates at different time points after 15 Gy SDRT, and tumors were removed 2 minutes later to assess Hoechst 33342 accumulation in the tumor interstitial space as a surrogate of perfusion/diffusion (21). Figure 1A shows progressive probe dec-

rement in B16F1 melanoma in $asmase^{+/+}$ (WT) mice beginning 5 minutes after SDRT, and pixel-by-pixel composite of whole-section mounts of B16F1 melanomas and MCA/129 fibrosarcomas revealed perfusion nadirs at 15–30 minutes after 15 Gy (Figure 1B; $P < 0.05$ vs. unirradiated each), followed by perfusion recovery. Perfusion reduction was not observed in either tumor implanted in vascular injury–inert $asmase^{-/-}$ littermates. Similarly, dynamic contrast–enhanced MRI–derived (DCE-MRI–derived) Ak_{ep}, a quantitative surrogate of microvascular flow/perfusion of tumor tissue (22), showed perfusion attenuation in intact B16F1 melanomas in WT but not $asmase^{-/-}$ hosts (Figure 1C and Supplemental Figure 1A; supplemental material available online with this article; https://doi.org/10.1172/JCI97631DS1) at 30 minutes after 20 Gy SDRT. Composite whole-tumor Ak_{ep} reconstruction (Figure 1D) revealed 67% ± 10% perfusion reduction in B16F1 melanomas in WT hosts compared with 23% ± 13% in $asmase^{-/-}$ littermates ($P < 0.05$). Comparable responses occurred in MCA/129 fibrosarcomas (Supplemental Figure 1, A and B) and in MCa mammary carcinoma tumors in C3H/HeJ mice (Supplemental Figure 2, A and B).

SDRT also induced functional alteration in tumor oxygenation, assessed by measurement of partial oxygen pressure (pO_2) within the tumor core of MCA/129 fibrosarcomas and B16F1 melanomas using the luminescence-based OxyLite method (23, 24). The OxyLite system, which provides pO_2 readouts every 10–30 seconds within a constant tumor subvolume before, during, and after SDRT exposure (Supplemental Figure 3, A–D), revealed pO_2 decreases within 30 minutes of 15 Gy SDRT of MCA/129 fibrosarcomas in $asmase^{+/+}$ WT hosts from 32.8 ± 2.8 to a hypoxic nadir of 10.0 ± 1.4 mmHg (Figure 1E; $P < 0.0001$), compared with no hypoxic response in tumors in $asmase^{-/-}$ littermates (28.3 ± 4.5 vs. 32.5 ± 4.0 mmHg, respectively; $P = 0.09$). Similar pO_2 changes were found in B16F1 melanoma exposed to 20 Gy SDRT (Supplemental Figure 3, E and F). To explore whether reduction in tumor pO_2 occurring in WT hosts was associated with ASMase-mediated vasoconstriction, we used the selective endothelin-1A receptor (ET_AR) antagonist BQ-123, which competitively inhibits vasoconstrictor endothelin-1 binding to ET_AR (25) and aborts the ischemic phase of I/R in experimental myocardial infarction (26). Whereas endothelial cells lack ET_AR (26), BQ-123 does not directly impact endothelial ASMase-initiated signal transduction. Figure 1E and Supplemental Figure 3C show that tumor pretreatment with BQ-123 aborted the acute hypoxic response to 15 Gy SDRT (pO_2 of 26.6 ± 3.5 mmHg before vs. 28.9 ± 4.1 mmHg after SDRT; $P = 0.13$). Thus SDRT produces a massive, previously unrecognized ASMase-mediated I/R injury in tumors within 1 hour, preceding detectable evidence of SDRT-induced endothelial apoptosis. Notably, pO_2 reduction appears to be restricted to tumors, as Supplemental Figure 4, A–C, reports that normal-tissue microvascular function after SDRT, using DCE-MRI and OxyLite pO_2 measurements, was unaffected in normal skin, subcutaneous tissue, and striated muscle of sv129/BL6 mice, sites within the radiation field in the current studies.

Acute I/R injury is induced in human tumors following 24 Gy SDRT. To explore perfusion changes in human cancer, we used intravoxel incoherent motion (IVIM) diffusion-weighted MRI (DW-MRI), which allows acquisition of multiple measurements over time without administration of intravenous contrast medi-
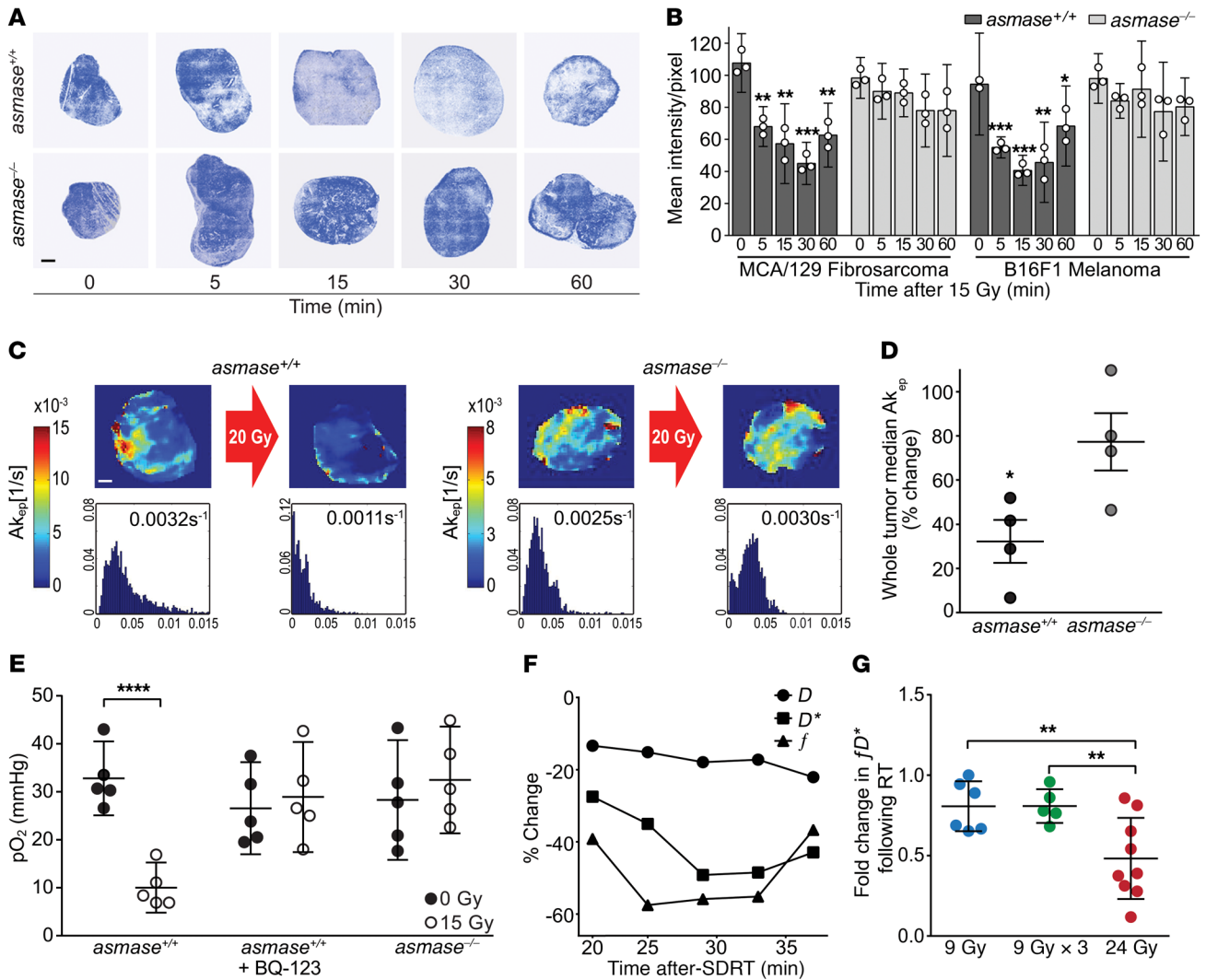
Figure 1. SDRT induces I/R in tumor microvasculature. (**A**) Representative fluorescent Hoechst 33342 accumulation in the interstitial space of fresh-frozen sections of B16F1 melanoma, injected at indicated times after 15 Gy SDRT; tumors were removed 2 minutes later. Blue regions are perfused and white regions are hypoxic. Scale bar: 1 mm. (**B**) Tumor perfusion reconstructed from whole-section mounts of tumors exposed to 15 Gy SDRT, quantified pixel by pixel by Hoechst 33342 fluorescence intensity. Data represent mean ± 95% CI collated from 2–3 mice per time point. *$P < 0.05$, **$P < 0.01$, ***$P < 0.001$, vs. unirradiated controls, Bonferroni correction (threshold: $\alpha = 0.05/4 = 0.0125$). (**C**) Tumor perfusion assessed by DCE-MRI–derived Ak_{ep} in B16F1 melanomas before and 30 minutes after 20 Gy SDRT. Color-coded Ak_{ep} intensity heatmaps (top) and respective Ak_{ep} histograms (bottom) are quantified pixel by pixel across a representative 1-mm DCE-MRI slice, expressed as median Ak_{ep} values. Scale bar: 1 mm. (**D**) Each dot represents perfusion reduction from 1 mouse implanted with B16F1 melanoma, reconstructed from whole-tumor Ak_{ep} histograms normalized to preradiation values (4 mice per group). Data represent mean ± SEM. *$P < 0.05$. (**E**) Effect of SDRT on MCA/129 fibrosarcoma pO_2 quantified by the OxyLite method. Data represent mean ± 95% CI before versus 30 minutes after 15 Gy SDRT (5 mice per group). ****$P < 0.0001$ vs. unirradiated, paired 2-tailed t test. (**F**) DW-MRI–derived IVIM coefficients in a patient receiving 24 Gy SDRT for primary prostate cancer. Time-dependent changes of f and D^* register I/R after SDRT. (**G**) Fold changes in fD^* in oligometastatic bone lesions exposed to 24 Gy SDRT, 9 Gy or 3×9 Gy radiotherapy. Data represent mean ± SD of 16 repeat fD^* values per point. **$P < 0.01$, Bonferroni correction (threshold: $\alpha = 0.05/2 = 0.025$).

um, yielding 3 parameters: f, which quantitates microvascular blood volume; pseudo-diffusion D^*, which estimates blood flow velocity; and D, which evaluates tissue cellular density (ref. 27 and Supplemental Figure 5, A and B). Figure 1F shows an IVIM DW-MRI study registering a time-dependent decrease in f and D^* values after 24 Gy SDRT in a single prostate cancer patient with nadirs of 55% at 25 minutes and 49% at 30 minutes, respectively, indicating a post-SDRT ischemic phase, followed by reperfusion. Similar decrements were observed in another 2 patients (Supplemental Table 1), but not in 2 patients exposed to 5 hypofraction-

ated doses of 9 Gy, a dosage below the 10-Gy ASMase activation threshold (14). Similarly, in an IRB-approved addendum to protocol NCT01223248 (ClinicalTrials.gov), prospectively randomized patients with human oligometastatic bone lesions were treated with 24 Gy SDRT or 3 hypofractionated daily 9-Gy fractions, and underwent IVIM DW-MRI imaging before and within 20–45 minutes (mean 26 minutes) after treatment, quantifying tumor perfusion as the product fD^* (27). The IVIM DW-MRI data revealed a mean 52% reduction in perfusion in the 24-Gy SDRT cohort, not observed in the 9-Gy cohort (Figure 1G; $P < 0.01$). Notably,

while the fD^* product best correlates IVIM perfusion with DCE-MRI estimates (27), separate analysis of f and D^* in the 24-Gy group revealed mean tumor reductions of 37% and 33% ($P < 0.05$ and $P < 0.01$, paired 2-tailed t test), respectively (Supplemental Table 2), not detected in the 6 patients treated with 9 Gy or the 6 treated with 3×9 Gy. These results provide evidence of mouse-to-human translation of a critical element of the new SDRT biology discovered here.

I/R injury, not endothelial apoptosis, impairs DSB repair. To assess whether SDRT-induced I/R injury (termed SDRT-I/R), endothelial apoptosis, or both impact the DDR in parenchymal tumor cells, we quantified resolution kinetics of γH2AX repair foci, the biomarker of choice for assessing global DSB repair in vivo (28). Foci colocalizing γH2AX with MDC1 and/or 53BP1 are considered specific for DSB repair, formed within minutes of DSB induction and resolving once DSB repair is accomplished. Disruption of repair attenuates focus resolution, rendering increased γH2AX foci during early-phase (3–8 hours) DDR, and residual γH2AX foci at ≥24 hours after regulated DDR functions terminate (28), indicative of unrepaired or misrepaired lesions. Control experiments using MCA/129 fibrosarcomas and B16F1 melanomas showed γH2AX/53BP1 focus accrual by 30 minutes after 2 Gy, and early resolution kinetics were similar in tumors in WT and *asmase*$^{-/-}$ littermates (Supplemental Figure 6A) with more than 95% of 53BP1 colocalizing with γH2AX (not shown), consistent with published data (28). However, while initial foci numbers at 30 minutes after 15 Gy were similar in tumors in both host strains (Figure 2A, right panel of each set), focus resolution was attenuated in tumors in WT hosts between 3 and 8 hours ($P < 0.05$ each), rendering a persistent difference at 24 hours (not shown), indicating impaired DSB repair in WT relative to *asmase*$^{-/-}$ hosts. Furthermore, while, within the sub-SDRT range of 2–8 Gy, γH2AX foci per nucleus were quantitatively similar at 6 hours in WT and *asmase*$^{-/-}$ littermates (Figure 2A, left panel of each set), at ≥10 Gy, the threshold for ASMase-driven endothelial injury (14), the curves diverge, showing increased γH2AX foci in tumors in WT littermates ($P < 0.05$ each >10 Gy). Similar attenuated focus resolution was observed in HCT116 xenografts in WT hosts (Figure 2B; $P < 0.05$ each), and in MCa mammary carcinoma tumors in C3H/HeJ mice (Supplemental Figure 2C). Hence these data correlate impaired DSB repair with induction of microvascular dysfunction in 4 different SDRT-treated mouse tumor models: MCA/129 murine fibrosarcomas in sv129/BL6 mice, HCT116 human colorectal carcinomas in B6.CB17-Prkdcscid/SzJ (SCID) mice, B16F1 murine melanomas in C57BL/6J mice, and MCa mammary carcinomas in C3H/HeJ mice.

To evaluate whether I/R per se impairs DSB repair, mechanical I/R was employed in I/R-inert *asmase*$^{-/-}$ hosts by a 2-minute percutaneous clamp of large tumor-feeding vessels immediately after SDRT, followed by clamp release, a protocol that activates I/R biology in myocardial tissues (29). To validate that the clamp method used here is effective in conferring hypoxia, we used the OxyLite system to measure pO$_2$ in MCA/129 fibrosarcoma in vivo. Measurements were performed at 10-second intervals for 20 minutes before, during, and after the 2-minute clamp. We observed a marked drop of pO$_2$ from baseline of 11.3, 15.8, and 26 mmHg in 3 mice, respectively, to undetectable in each, followed by recovery to baseline pO$_2$ within 5–10 minutes after clamp release. Nota-

bly, while the 2-minute tumor clamp reaches hypoxic levels faster than SDRT, which requires at least 5 minutes after radiotherapy to reach maximal hypoxia (Supplemental Figure 3A), nonetheless both reach ≤10 mmHg, the hypoxic level considered requisite for the pathophysiologic effect of acute hypoxia (24, 30). Clamping did not impact tumor growth or postclamp perfusion in unirradiated controls, nor did it induce endothelial apoptosis (not shown). However, immediate postirradiation clamping (designated C) of tumors in *asmase*$^{-/-}$ (KO) hosts attenuated γH2AX, MDC1, and 53BP1 focus resolution (Figure 2C for HCT116 tumors, $P < 0.0001$ each vs. WT; and Supplemental Figure 6B for MCA/129 fibrosarcomas and B16F1 melanomas, $P < 0.001$ and $P < 0.0001$ KO vs. KO+C, respectively), restoring the delayed resolution phenotype observed in WT hosts. Reversing the temporal sequence of SDRT and mechanical I/R by tumor clamping at 10 minutes before SDRT failed to alter kinetics of γH2AX focus resolution (Supplemental Figure 6C), nor did post-SDRT clamping affect focus resolution in WT I/R-replete *asmase*$^{+/+}$ hosts (Supplemental Figure 6D). These data suggest a temporal association between initiation of DSB repair and I/R injury that promotes DDR dysfunction after SDRT.

Antagonism of DSB repair by acute I/R injury was also validated using BQ-123 in WT hosts. BQ-123 pretreatment of HCT116 tumors in WT hosts enhanced γH2AX and MDC1 focus resolution at 6 hours after 15 Gy to rates comparable to those in I/R-inert *asmase*$^{-/-}$ hosts, evidenced in Figure 2C as reduced focus number at 6 hours, while postradiation clamping reversed the BQ-123 effect (Figure 2C; $P < 0.0001$ vs. WT). Similar BQ-123 effects were registered at 3 and 8 hours after irradiation (not shown) and in MCA/129 fibrosarcomas (Supplemental Figure 6B). Hence, quantitative assessment of global DSB repair, defined by the DDR dysfunctional focus resolution phenotype induced by SDRT-I/R, can be recapitulated by mechanical I/R in I/R-inert tumors, while genetic or pharmacologic silencing of I/R appears to reveal the repair potential of the inherent DDR in exposed tumor cells unperturbed by I/R.

While these data support I/R as initiator of impaired tumor cell DSB repair, BQ-123 at a dose that effectively inhibited I/R and conferred proficient DSB repair (Figure 2C and Supplemental Figure 6B) did not concomitantly alter endothelial apoptosis after 15 Gy SDRT (Figure 2D; $P = 0.7$), dissociating ASMase-dependent endothelial apoptosis from I/R-mediated DDR dysfunction in tumor parenchymal cells.

I/R injury represses SUMOylation to confer epigenetic HDR loss of function. To identify the repair pathway affected by I/R injury, we delineated engagement of NHEJ and HDR mediators in tumors exposed to SDRT. We found canonical Ku-dependent NHEJ to be insensitive to the vascular component of SDRT. MCA/129 fibrosarcomas and B16F1 melanomas (Figure 3A) in I/R-competent *asmase*$^{+/+}$ and I/R-incompetent *asmase*$^{-/-}$ littermates accrued and resolved DNA-PKcs and XRCC4 foci similarly. In contrast, focus resolution of 53BP1, a multifunctional DDR mediator that antagonizes HDR and promotes NHEJ of DSBs (31), was significantly attenuated in HCT116 xenografts in WT hosts (Figure 2, B and C), as well as in MCA/129 fibrosarcomas and B16F1 melanomas in WT hosts (Supplemental Figure 7A), compared with *asmase*$^{-/-}$ littermates, coincident with delayed MDC1 focus resolution (Figure 2, B and C). MDC1 focus resolution is initiated by SUMO2/3 conjugation, promoting binding of the SUMO-targeted E3 ubiqui-
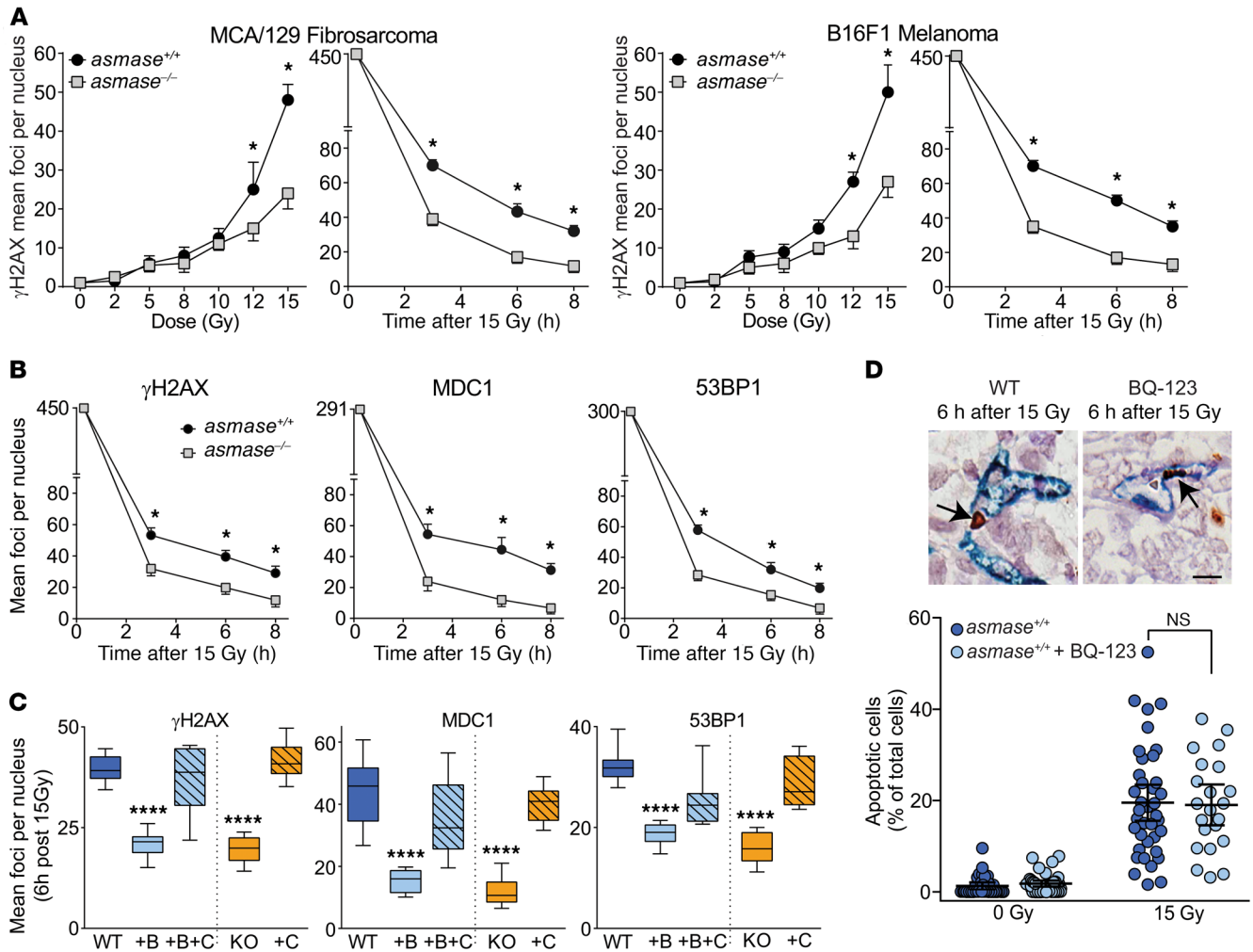
Figure 2. I/R, not endothelial apoptosis, impairs DSB repair. (**A**) Time-dependent (after 15 Gy) and dose effects (registered at 6 hours after radiation) on γH2AX focus resolution after SDRT in MCA/129 fibrosarcomas (left panel) and B16F1 melanomas (right panel). Each data point represents mean ± SEM (2–4 tumors) with high-power microscopic fields scanned for each time/dose focus count. (**B**) Kinetics of γH2AX, MDC1, and 53BP1 focus resolution in HCT116 xenografts after 15 Gy SDRT. (**A** and **B**) Data represent mean ± SEM. *$P < 0.05$ *asmase*^{+/+} (designated WT) vs. *asmase*^{−/−} (designated KO) tumor host. (**C**) Impact of mechanical I/R on focus resolution in HCT116 xenografts at 6 hours after 15 Gy SDRT. Mechanical percutaneous clamping (designated C) of large tumor-feeding vessels was applied immediately after SDRT in I/R-inert BQ-123–inhibited tumors in *asmase*^{+/+} (WT) hosts or tumors in *asmase*^{−/−} (KO) hosts. BQ-123 (designated B) was injected i.p. (2 mg/kg) at 30 minutes before SDRT. Data represent median ± IQR. ****$P < 0.0001$, B and KO vs. WT, Bonferroni correction (threshold: α = 0.05/4 = 0.0125). (**D**) Tumor pretreated with BQ-123 fails to impact SDRT-induced endothelial apoptosis. Representative apoptotic endothelial cells (arrows) double-stained with pan-endothelial MECA-32 (blue) and TUNEL (brown) in irradiated MCA/129 fibrosarcoma (top), quantified (bottom) in HCT116 tumor xenografts in *asmase*^{+/+} hosts. Data represent mean ± 95% CI, $P = 0.7$. Scale bar: 20 μm. Data are collated from 2 × 10³ to 4 × 10³ nuclei per point using 3–5 mice per group in **A**–**C**, and from 6 mice per group in **D**.

tin ligase RNF4, MDC1 ubiquitination, and proteasomal degradation (32). Genetic inhibition of MDC1 SUMO2/3-ylation abrogates MDC1-RNF4 coupling and delays MDC1 focus resolution, with coordinate delayed 53BP1 focus resolution (33). The observed attenuation of MDC1/53BP1 focus resolution after SDRT-I/R raises the question of whether SDRT-I/R might also be associated with SUMO2/3 focus dysfunction.

In this context, we found that 15 Gy SDRT induced time-dependent increase of SUMO2/3 focus–positive nuclei in I/R-inert HCT116 tumors in *asmase*^{−/−} hosts, beginning at 1 hour and peaking at 6 hours (Figure 3B), attenuated at all times in SDRT-I/R–conditioned tumors in *asmase*^{+/+} littermates ($P < 0.05$ each). Quantitatively, SDRT-I/R reduced HCT116 SUMO2/3 foci at 6

hours after 15 Gy to approximately 35% of the level in I/R-inert tumors (Figure 3C; $P < 0.001$ vs. WT). A similar SUMO2/3 phenotype was observed in MCA/129 fibrosarcomas (Supplemental Figure 7B) and in MCa mammary carcinomas (Supplemental Figure 2D). Notably, 8 Gy, a subthreshold dose for I/R injury, did not attenuate SUMO2/3 focus accrual in WT hosts (Supplemental Figure 7C, top). Furthermore, the patterns of focus recruitment of the E3 SUMO ligase PIAS1, required for SUMO2/3 conjugation of BRCA1, and focus recruitment of BRCA1 itself, mimic that of SUMO2/3 in WT and *asmase*^{−/−} hosts, respectively (Figure 3B and Supplemental Figure 7C, bottom). Whereas multiple HDR mediators were reported to be activated by SUMO2/3 conjugation (32), occurring as a DDR-coordinated group response (34), we found
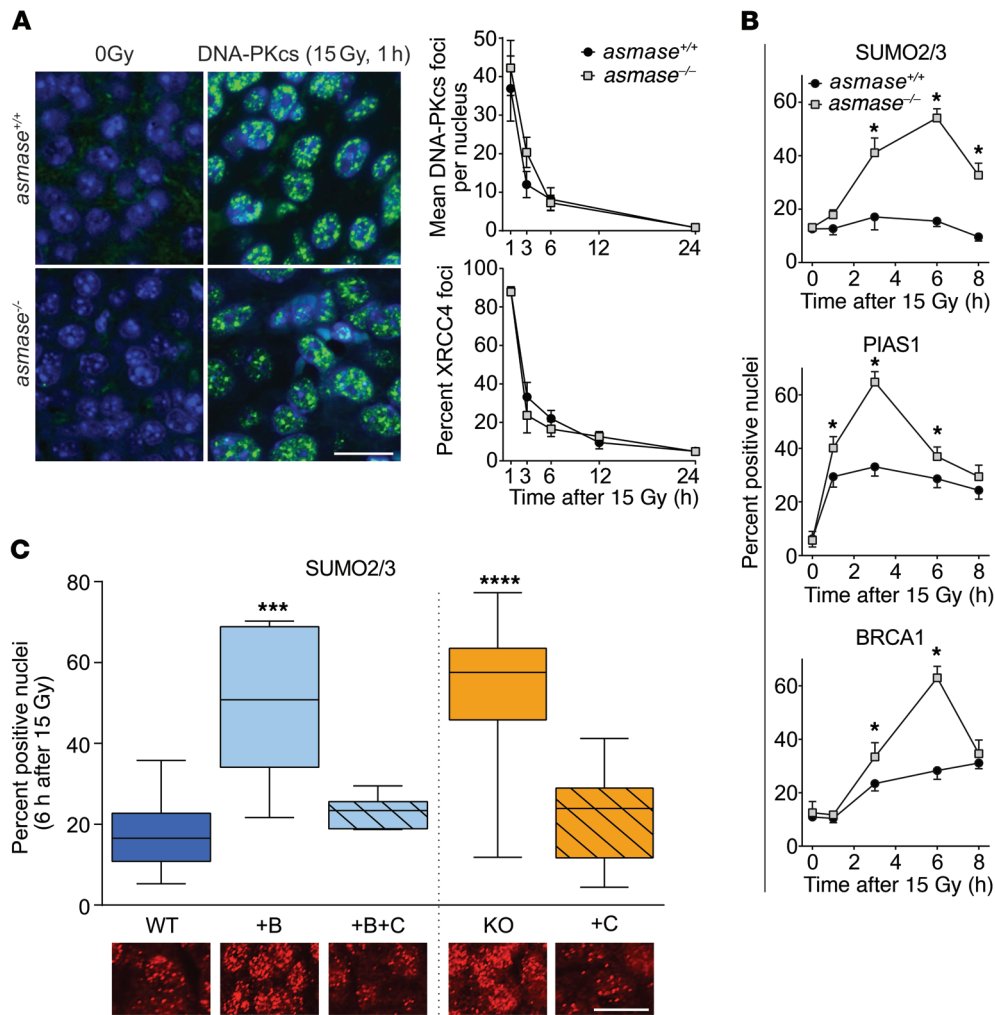
Figure 3. I/R confers epigenetic HDR loss of function. Foci were scored as in Figure 2 in *asmase*^{+/+} (WT) or *asmase*^{−/−} (KO) hosts. (**A**) Canonical NHEJ is insensitive to SDRT-I/R. Left: Representative DNA-PKcs foci in MCA/129 fibrosarcomas 1 hour after 15 Gy SDRT. Right: Time-dependent change in DNA-PKcs and XRCC4 foci in SDRT-treated B16F1 melanomas. Scale bar: 20 μm. Data represent mean ± SEM collated from 2–4 independent experiments per panel of 3 mice per group. *P* > 0.05, WT vs. KO. (**B**) Time course of SUMO2/3, PIAS1, and BRCA1 focus accrual/resolution after 15 Gy SDRT in HCT116 xenografts. *P < 0.05, WT vs. KO unpaired *t* test. Data represent mean ± SEM collated from 2–4 independent experiments per panel of 3 mice per group. *P < 0.05, WT vs. KO. (**C**) Effects of SDRT-I/R injury (WT, WT+B+C, KO+C) versus SDRT-inert (WT+B, KO) settings on SUMO2/3 foci formation in HCT116 tumor xenografts at 6 hours after 15 Gy SDRT. BQ-123 (designated B), when used, was injected i.p. 30 minutes before SDRT, while mechanical percutaneous clamp (designated C) of large tumor-feeding vessels was used immediately after SDRT. Data represent median ± IQR percent foci-positive nuclei in tumor-derived histological specimens from 2–4 mice each, scoring a total of 2 × 10³ to 7 × 10³ HCT116 cells. ***P < 0.001, ****P < 0.0001 vs. WT, with Bonferroni correction (threshold: α = 0.05/4 = 0.0125). Inset shows representative SUMO2/3 focus images in respective SDRT-I/R–conditioned and I/R-inert. Scale bar: 20 μm.

that the upstream HDR mediators RAP80 and BRCA1, the efferent HDR proteins RPA and RAD51, and the SUMO-targeted E3 ubiquitin ligase RNF4, all of which require SUMO2/3 conjugation for focus assembly (32), closely mimicked the pattern of SUMO2/3 focus formation at 6 hours after 15 Gy in SDRT-I/R–conditioned and SDRT-inert tumor settings (Table 1; *P* < 0.05 vs. WT for each mediator in SDRT-I/R vs. I/R-inert settings). Similar impact of I/R-conditioned and I/R-inert settings on BRCA1 and RAD51 focus formation was observed in MCA/129 fibrosarcomas (Supplemental Figure 7D), B16F1 melanomas (Supplemental Figure 7E), and MCa mammary carcinomas (Supplemental Figure 2D). Together, these correlated responses are consistent with a model in which SDRT-I/R–mediated SUMO2/3-ylation loss of function globally represses function of the HDR toolkit. Notably, BRCA1 and RAD51

protein levels were similar in tumors in *asmase*^{+/+} and *asmase*^{−/−} mice before and after SDRT (Supplemental Figure 7F).

Deficiency of SUMO3, but not SUMO2, confers HDR loss of function. Subsequent studies explored SDRT-I/R effects on SUMO2/3 intermediary metabolism. Exposure of mammalian tissues to I/R triggers the adaptive SSR (18, 19) during ischemia via mitochondrial complex III O$_2$ sensors that respond to deep hypoxia with adaptive ROS generation (35). SSR displays a typical signature of high-MW-band (>75 kDa) SUMO-protein complexes, sustained for several hours after I/R injury (36). Figure 4A shows that the SSR signature occurred in MCA/129 fibrosarcomas in WT but not in *asmase*^{−/−} hosts exposed to 20 Gy SDRT nor in MCA/129 fibrosarcomas in WT hosts exposed to 8 Gy subthreshold I/R (Supplemental Figure 8A). Mechanical I/R via 2-minute tumor vascular clamp

Table 1. I/R induces global dysfunction of HDR

	asmase^{+/+} (WT)	asmase^{+/+} + BQ-123 (+B)	asmase^{+/+} +BQ-123 + clamp (+B+C)	asmase^{-/-} (KO)	asmase^{-/-} + clamp (+C)
SUMO2/3	17.5 (± 2.6)	49.3 (± 5.6)[B]	23.2 (± 1.5)	51.9 (± 5.3)[B]	21.6 (± 3.3)
RNF4	25.2 (± 6.5)	57.0 (± 6.5)[A]	29.5 (± 2.9)	62.3 (± 7.9)[A]	26.0 (± 4.6)
RAP80	26.0 (± 2.6)	61.6 (± 1.9)[D]	23.2 (± 3.7)	62.8 (± 3.2)[D]	23.4 (± 3.3)
BRCA1	21.7 (± 3.9)	56.9 (± 3.7)[C]	24.1 (± 1.7)	63.3 (± 3.1)[C]	24.5 (± 3.0)
RPA32	24.8 (± 2.9)	37.6 (± 2.3)[A]	22.8 (± 2.6)	39.7 (± 3.7)[A]	27.9 (± 1.7)
RAD51	17.2 (± 1.8)	43.0 (± 3.0)[C]	22.5 (± 2.5)	42.2 (± 9.1)[A]	21.0 (± 4.7)

Accrual of principal HDR mediators and effectors into DSB repair foci were scored in 2×10^3 to 7×10^3 HCT116 nuclei per tumor at 6 hours after 15 Gy SDRT. Data represent mean ± SEM percent positive nuclei from 2–4 mice per group. BQ-123 (B) was injected i.p. at 30 minutes before SDRT, while 2 minutes mechanical percutaneous clamp (C) of large tumor-feeding vessels was applied immediately after SDRT. [A]$P < 0.05$, [B]$P < 0.01$, [C]$P < 0.001$, [D]$P < 0.0001$, all groups vs. WT control, with Bonferroni correction (threshold: $\alpha = 0.05/4 = 0.0125$).

immediately after 20 Gy restored SSR in tumors in *asmase^{-/-}* mice (Figure 4A). The SSR high-MW band SUMO-protein complexes in SDRT-exposed fibrosarcomas engaged SUMO2/3 (Figure 4A), but not SUMO1 (not shown). Together, these data indicate that SSR is not induced by SDRT per se, but rather by consequent I/R injury.

Western blotting also disclosed that 30%–40% reduction of nonconjugated free SUMO2/3 occurred in 20 Gy–exposed tumors in WT hosts compared with unirradiated controls or tumors irradiated in *asmase^{-/-}* littermates (Figure 4A). Notably, antibodies used here detected free SUMO2/3 as an approximately 17-kDa–MW doublet, consistent with SUMO2 and SUMO3 sharing 97% sequence identity (37), with the upper minor band representing SUMO3 (Figure 4A; confirmed in Supplemental Figure 8B). Whereas we report reduced SUMO2/3 recruitment into chromatin DSB repair foci after SDRT-I/R (Figure 3, B and C), subcellular fractionation revealed that control unirradiated tumor cytoplasmic fractions displayed both free SUMO2 and SUMO3 proteins, while only SUMO3 was detected in control chromatin-enriched fractions (Figure 4B; $P < 0.01$ vs. unirradiated). Further, while cytoplasmic free SUMO2 and SUMO3 were unchanged in 20 Gy–treated tumors in *asmase^{+/+}* and *asmase^{-/-}* mice, chromatin-enriched free SUMO3 was 70% ± 6% depleted by 90 minutes after 20 Gy in tumors in *asmase^{+/+}*, but not *asmase^{-/-}*, hosts (Figure 4B). Concomitantly, progressive time-dependent accumulation of SSR high-MW (>75 kDa) SUMO-protein complexes occurred in cytoplasm after 20 Gy, absent in the chromatin-enriched fraction (Figure 4B), and not detected in *asmase^{-/-}* hosts.

To address the SUMO paralog regulating the HDR cluster, we transduced cultured HCT116 cells with shSUMO2 or shSUMO3, yielding 75%–90% reduction in respective mRNAs (Supplemental Figure 9A) and SUMO proteins (not shown). While baseline cell growth was not affected in shSUMO-transfected cells (Supplemental Figure 9B), when irradiated (5 Gy) under standard aeration, significantly reduced growth (Figure 5A and Supplemental Figure 9C; $P < 0.05$ each), colony formation (Figure 5B), and γH2AX focus resolution (Figure 5C and Supplemental Figure 9D) occurred in shSUMO3, but not shSUMO2, cells, indicating that SUMO3-deficient cells display radiation hypersensitivity. Further, while no impairment of canonical NHEJ DNA-PKcs focus kinetics was detected in HCT116-shSUMO3 (Supplemental Fig-

ure 9E), significant reduction in accrual of RAP80, BRCA1, and RAD51 into repair foci occurred at 3–6 hours after 5 Gy, absent in HCT116-shSUMO2 or control shScrambled cells (Figure 5D), mimicking the SDRT-I/R phenotype of tumors in *asmase^{+/+}* hosts (Figure 6E, Supplemental Figure 2D, and Supplemental Figure 7, D and E). Thus SUMO3, but not SUMO2, appears to be required and sufficient for conjugation-dependent activation of HDR mediators, with resultant radiosensitization in its absence.

ROS mediate SUMO3 dysfunction to confer synthetic tumor cell lethality. While the mechanism of free SUMO3 depletion in chromatin remains unknown, oxidative damage to nuclear pore complex proteins was reported to disrupt nuclear retention of free SUMO1/2/3 (38, 39). Furthermore, recent studies report that exposure of tumor cells to acute deep hypoxia, such as is triggered by SDRT-I/R (Figure 1, A–E, and Supplemental Figures 1–3), is sensed by mitochondrial complex III, evoking ROS release from the electron transport chain into the affected cell cytosol, triggering an adaptive oxidant stress response (35, 40). To explore whether SDRT-I/R engages ROS, rendering SSR and chromatin SUMO3 depletion, we explored whether pharmacologic or genetic antioxidant strategies might abort SSR/SUMO3 pathology, reversing HDR loss of function. We used stable overexpression of peroxiredoxin-6 (Prdx6) (41) in MCA/129 fibrosarcoma tumors, or systemic application of the SOD-mimetic antioxidant scavenger tempol (42) injected intraperitoneally at 30 minutes after SDRT, the estimated peak of SDRT-I/R hypoxia. The peroxiredoxin antioxidant superfamily is ubiquitously expressed in mammalian tissues, possessing a structure that renders cysteine residues at the active site highly sensitive to oxidation by H_2O_2 (43). Prdx6 is unique in this group, containing a single conserved cysteine that co-opts glutathione, rather than thioredoxin, to catalyze peroxide reduction. Consistent with a key role for Prdx6 in antioxidant defense, cells, tissues, or mice with an inactivated or depleted Prdx6 gene exhibit increased sensitivity to oxidative stress, while mice overexpressing Prdx6 are ROS resistant (41).

We initially evaluated intensity of SDRT-induced ROS production in MCA/129 fibrosarcomas exposed to 20 Gy SDRT using dihydroethidium (DHE) to trap ROS (44). When oxidized by ROS, DHE converts into ethidium bromide, which is rapidly intercalated into DNA and emits a red fluorescent signal that can be used to
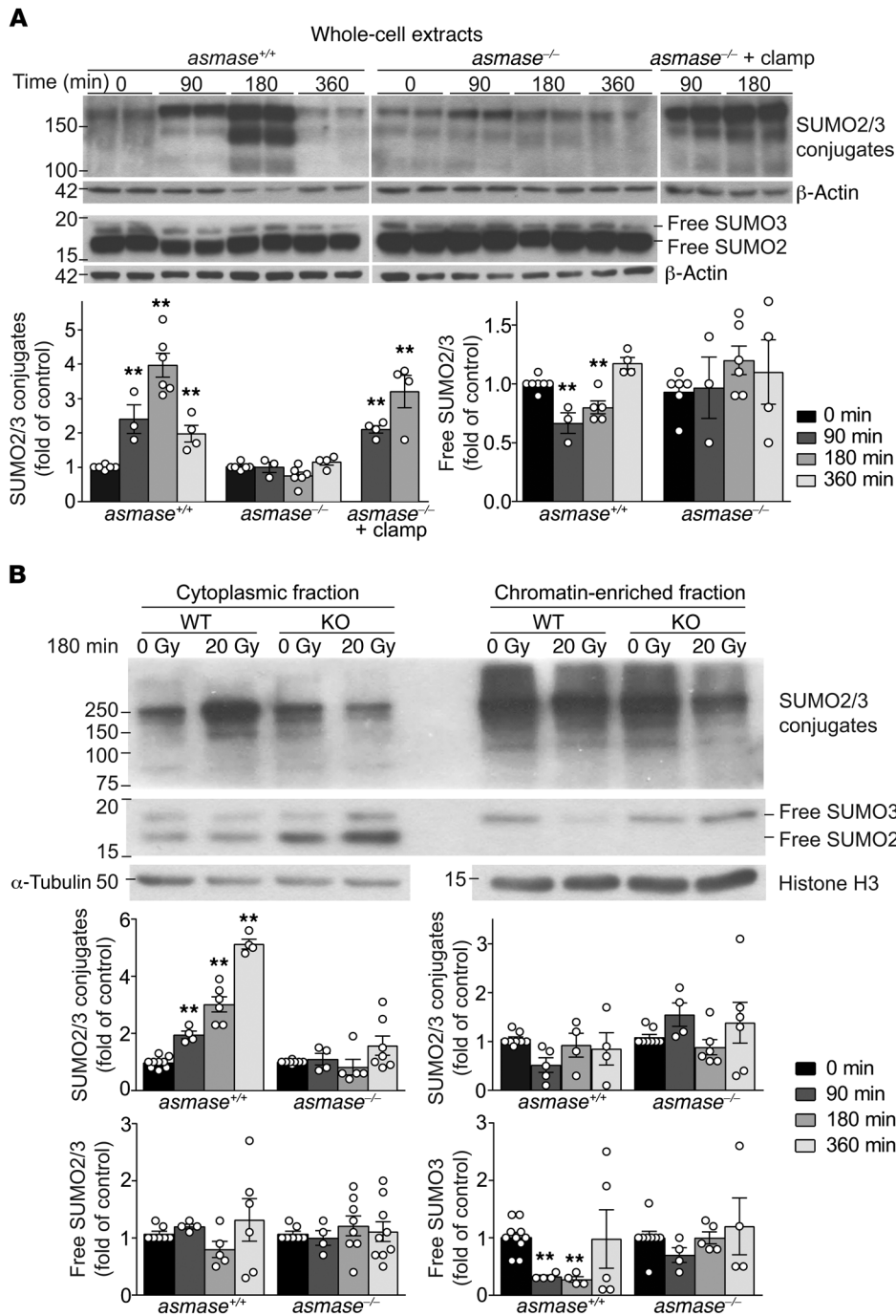
Figure 4. I/R disrupts SUMO2/3 function in tumors exposed to SDRT. Western blot (WB) analysis of tumor extracts using rabbit polyclonal anti-SUMO2/3 antibody, quantified by densitometry relative to loading controls. (**A**) Whole-cell extracts from MCA/129 fibrosarcoma in *asmase*^{+/+} and *asmase*^{−/−} hosts after 20 Gy SDRT. Top panels show representative WBs, and bottom panels quantify high-MW SUMO2/3 conjugates (>75 kDa) and free SUMO2/3. (**B**) Representative WBs of high-MW SUMO2/3 conjugates (>75 kDa) and free SUMO2/3 in cytoplasmic (left) and chromatin-bound (right) fractions isolated from MCA/129 fibrosarcomas in *asmase*^{+/+} and *asmase*^{−/−} hosts at 3 hours after 20 Gy SDRT. Bottom panels show quantitative analysis of specimens at different times after 20 Gy. (**A** and **B**) Data represent mean ± SEM of at least 3 independent experiments of 2 mice per group. **$P < 0.01$ vs. 0min, Bonferroni correction (threshold: $\alpha = 0.05/3 = 0.017$).

quantify ROS (44). Figure 6A shows that SDRT-I/R increases ROS production 3.2 ± 0.8–fold in MCA/129 fibrosarcomas by 1 hour after 20 Gy ($P < 0.05$), aborted by BQ-123 pretreatment and effectively scavenged by tempol. Consequently, Prdx6 overexpression (Supplemental Figure 10, B and C) or systemic tempol delivered at 30 minutes after 20 Gy SDRT aborted the SSR in MCA/129 fibrosarcomas in WT hosts (Figure 6B), preventing free chromatin-associated SUMO3 depletion (Figure 6C), reverting delayed γH2AX/MDC1 focus resolution, and restoring tumor cell HDR as assessed by the increase of SUMO2/3, BRCA1, and RAD51 focus formation to levels in I/R-inert tumors in *asmase*^{−/−} hosts (Figure 6, D and E, and Supplemental Figure 10, D and E; $P < 0.01$ vs. WT). Together,

these data confirm a critical role for I/R-induced ROS in induction of SUMO3-mediated HDR dysfunction in SDRT-exposed tumors.

To explore whether ROS-mediated epigenetic HDR loss of function associates with lethal chromosomal damage, we quantified micronuclei (MN; typical lesions in Figure 6F) during the first post-SDRT mitotic cycle using an ex vivo cytokinesis-blocking MN assay (45). We found that 85% ± 4% of MCA/129 fibrosarcoma cells derived from tumors in *asmase*^{+/+} hosts versus 38% ± 3% in *asmase*^{−/−} littermates contained binucleate MN at 48 hours after 15 Gy (Supplemental Figure 11A; $P < 0.0001$ and $P < 0.01$, WT and KO+C vs. KO). Postradiation clamp of tumors in *asmase*^{−/−} hosts increased MN (Supplemental Figure 11A). Similar responses
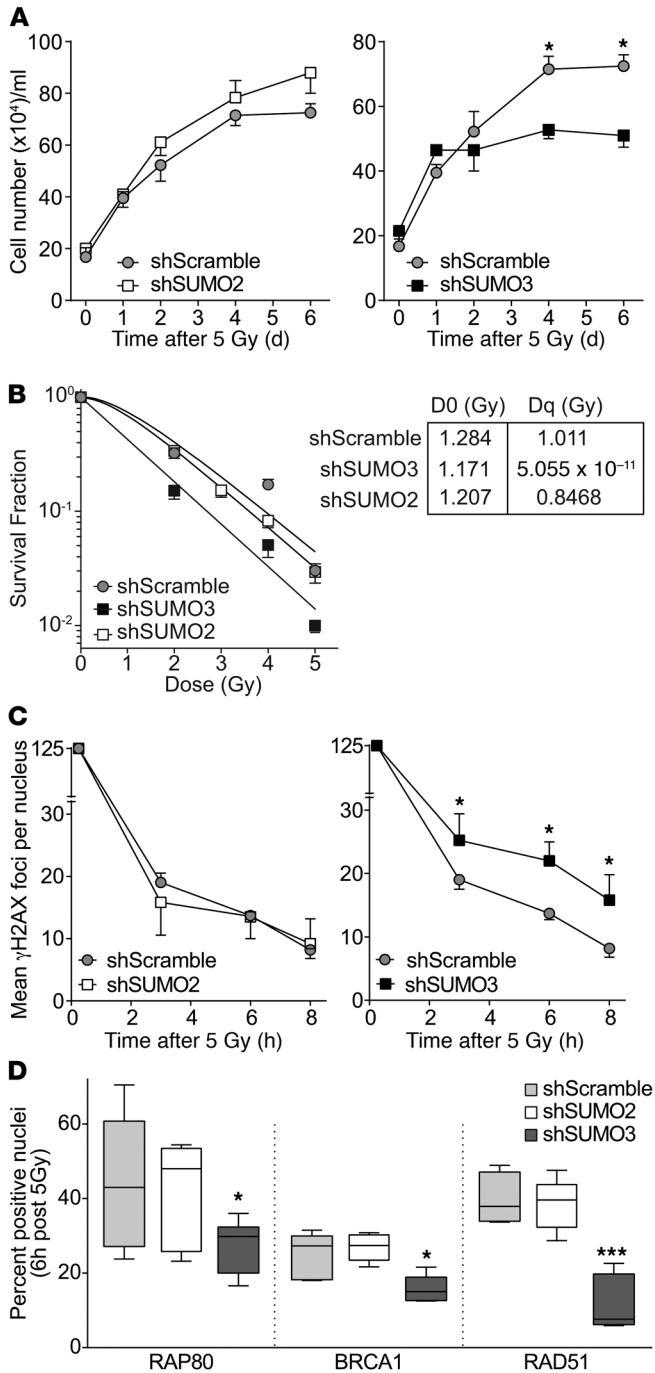
Figure 5. SUMO3, not SUMO2, is required for conjugation-dependent activation of HDR mediators. (**A**) Growth curves of shScramble-, shSUMO2-, and shSUMO3-transduced HCT116 cells after 5 Gy. Data represent mean ± SEM from 2 independent experiments performed in triplicate. (**B**) Clonogenic survival assay of transduced cells exposed to escalating SDRT doses. The inset provides the mathematically derived D0 and Dq coefficients of the dose-survival curves, defining the relative radiosensitivity of each cell line and the capacity to repair potentially lethal damage, respectively. Data represent mean ± SEM collated from 3 independent experiments performed in triplicate. (**C** and **D**) γH2AX focus resolution at 3–8 hours (**C**) and RAP80, BRCA1, and RAD51 accrual into repair foci at 6 hours (**D**) after 5 Gy in shSUMO2- or shSUMO3-expressing HCT116 cells. (**C** and **D**) Data represent median ± IQR from 2 independent experiments performed in triplicate. (**A** and **C**) *$P < 0.05$ vs. shScramble. (**D**) *$P < 0.05$, ***$P < 0.001$ vs. shScramble, with Bonferroni correction (threshold: $\alpha = 0.05/2 = 0.025$).

were observed in B16F1 melanomas (not shown). Increased MN can also be detected histologically in formalin-fixed mammalian specimens without blocking of cytokinesis (46), increasing 20-fold at 24 hours after 15 Gy SDRT in tumors in WT (Figure 6F; $P < 0.05$ vs. WT unirradiated) but not in *asmase*$^{-/-}$ hosts (Figure 6F; $P = 0.15$ vs. KO unirradiated). Further, 2-minute vascular clamp of tumors in *asmase*$^{-/-}$ hosts immediately after radiation increased tumor cell MN 5.9-fold to levels detected in WT hosts (Figure 6F; $P < 0.01$), while tempol abrogated the WT MN response, confirming that SDRT-I/R–induced ROS mediate generation of potentially lethal chromosomal aberrations. B16F1 melanomas exhibited similar responses (Supplemental Figure 11B). Critically, 27 Gy SDRT eradicated 8 of 17 (47%) MCA/129 fibrosarcomas, with the remaining tumors displaying initial tumor growth delay followed by resumption of exponential tumor growth at a rate similar to that in unirradiated tumor controls (Figure 6G). Systemic pre-SDRT treatment with BQ-123, or post-SDRT treatment with tempol, each reduced the local cure rate to 1/10 ($P < 0.05$, Fisher's exact test all 27 Gy, untreated vs. treated [BQ-123 or Tempol]). These studies also correlate tumor growth data at 27 Gy, the TCD$_{50}$ for MCA/129 fibrosarcomas, with 2 DSB markers (γH2AX and MDC1), and 2 DNA damage signaling markers (BRCA1 and RAD51), in the presence or absence of BQ-123 or tempol treatment (Supplemental Figure 12, A and B). At 27 Gy, we show a high incidence of DSB markers and a low incidence of DNA damage repair signaling markers, while the reciprocal is observed with use of the ET$_A$R antagonist BQ-123 and the ROS scavenger tempol that reduce tumor cure to 10%. These data indicate a tight correlation between recruitment of HDR repair enzymes to damaged DNA, repair of DSBs, and tumor control in the context of I/R injury (Supplemental Figure 12C).

Taken together, these data indicate that ROS generation is an indispensable mediator of SDRT-I/R pathobiology, conferring loss of function of chromatin-bound SUMO3 and HDR, rendering lethal chromosomal rearrangements, massive tumor cell lethality, and local tumor cure.

Discussion

While the present studies provide, to our knowledge, the first description of multiple elements of a new SDRT biology (Supplemental Figure 13), two events stand out as determinant for tumor ablation: the ASMase-driven perfusion defects and the consequent ROS/SSR–mediated HDR inactivation. Whereas radiation-induced ROS are known to generate DNA DSBs (47), the present data provide, to our knowledge, the first documentation of ROS inhibition of DSB repair. The observation that SUMO3, but not SUMO2, is mandatory for HDR activation despite 97% amino acid sequence homology (37), while unanticipated, is consistent with SUMO2 and SUMO3 differing in target selection (48, 49).

A body of literature provides a mechanism by which stress-induced endothelial ASMase activation triggers changes in microvascular function. SDRT (20, 50) or TNF superfamily receptor ligands (51, 52) induce translocation of ASMase residing in cytosolic secretory lysosomes to the outer plasma membrane within seconds to minutes, hydrolyzing external leaflet sphingomyelin to generate ceramide within microscopic liquid-ordered sphingomyelin/cholesterol–containing rafts (ref. 53 and Sup-
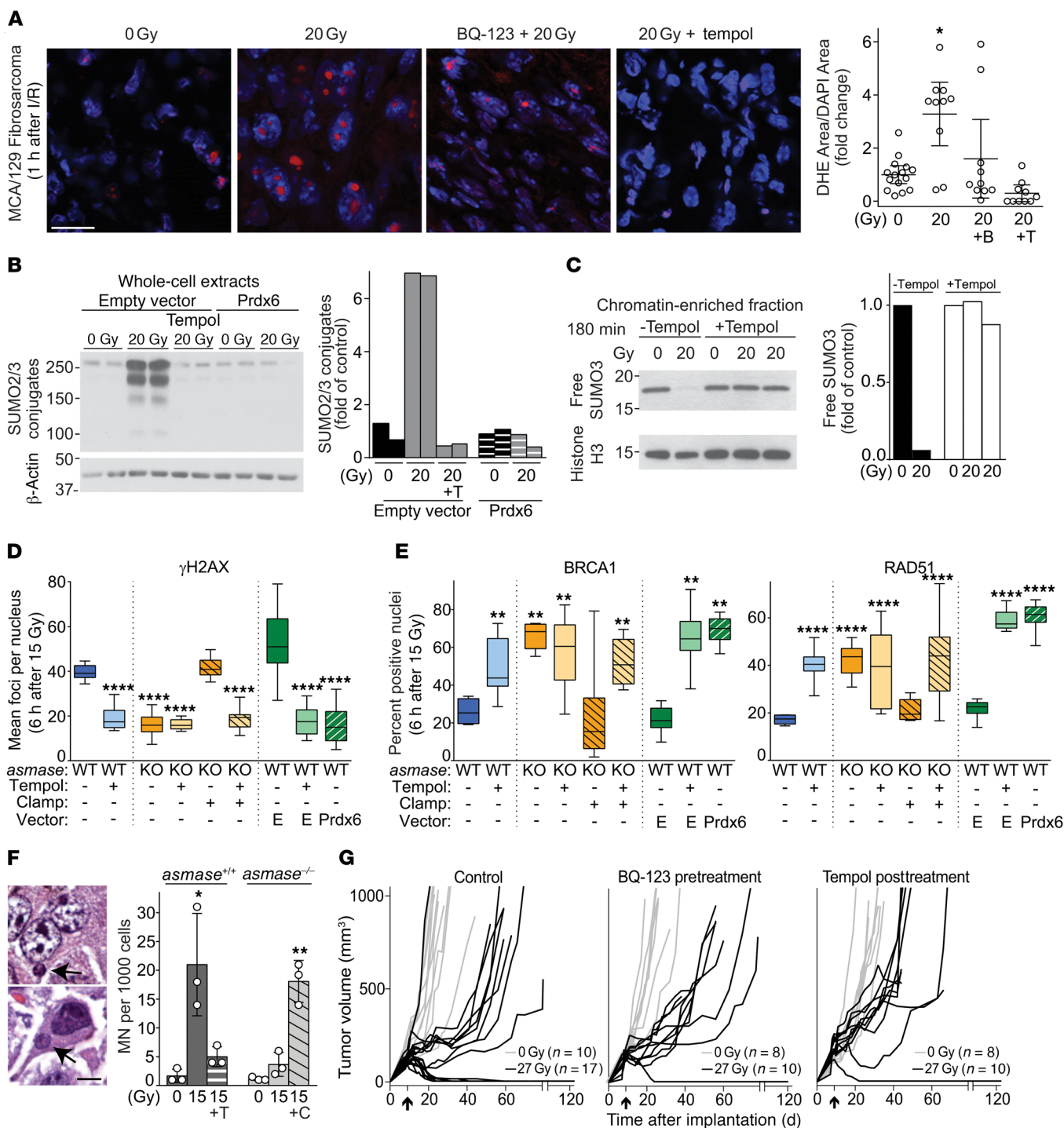
Figure 6. ROS mediate SUMO dysfunction and synthetic tumor lethality via the reproductive death pathway. (**A**–**E**) Experiments were performed using MCA/129 fibrosarcoma. Data were collated from 2–4 independent experiments using 2–4 mice per experiment. (**A**) Representative images (left; scale bar: 20 μm) and quantitation (right; data represent mean ± 95% CI) of dihydroethidium staining (DHE, red) and DAPI counterstaining (blue) of tumors in *asmase*$^{+/+}$ mice before and 1 hour after SDRT, with or without BQ-123 (designated B, 30 minutes before SDRT) or tempol (designated T, 30 minutes after SDRT). *$P < 0.05$, Bonferroni correction (threshold: $α = 0.05/3 = 0.017$). (**B**) Prdx6 overexpression or tempol abrogates the SSR induced by SDRT. Representative WBs of whole-cell lysates from tumors in *asmase*$^{+/+}$ (WT) mice. (**C**) Tempol abrogates chromatin-associated SUMO3 depletion. Representative WB of chromatin-enriched extract from tumors in *asmase*$^{+/+}$ mice. (**D** and **E**) Prdx6 overexpression or tempol abrogates delayed γH2AX focus resolution (**D**) and restores BRCA1 and RAD51 loading into repair foci (**E**) in SDRT-I/R–competent (WT or KO+C) tumors. Data represent median ± IQR. **$P < 0.01$, ****$P < 0.0001$ for all focus types vs. WT, Bonferroni correction (threshold: $α = 0.05/8 = 0.00625$). (**F**) Left: Representative images of micronuclei (MN; arrows) in H&E-stained tumor sections. Scale bar: 5 μm. Right: MN quantitation; data represent mean ± 95% CI from 3 independent experiments using 3 mice per group, 2,000 cells per tumor. *$P < 0.05$, **$P < 0.01$ for 15 Gy and 15 Gy + C vs. unirradiated WT, Bonferroni correction (threshold: $α = 0.05/4 = 0.0125$). (**G**) Ablation of MCA/129 fibrosarcomas in sv129/BL6 mice is aborted by pre-SDRT treatment with BQ-123 or post-SDRT treatment with tempol. Each line represents an individual tumor volume. Arrows indicate day of SDRT. Tumors undetectable at 120 days are considered cured.

plemental Figure 13). Once generated, ceramide spontaneously self-associates, coalescing lipid rafts into ceramide-rich platforms (CRPs), macrodomains that serve as sites of protein oligomerization for transmembrane signaling (53). Studies by Pin-Lan Li (54) reported that, once formed, endothelial CRPs promote assembly and activation of the NADPH oxidase (NOX) complex, generating superoxide radicals. Peroxynitrite generated from oxidation of the vasodilator NO uncouples dimeric endothelial NO synthase, temporarily reducing NO bioavailability. NO depletion unbalances homeostatic reciprocal NO/endothelin-1 coregulation of microvascular tonicity (55), yielding, upon reduction of the vasodilator NO, acute vasoconstriction via endothelin-1 stimulation of the endothelin-1A receptors (ET$_A$Rs) on arteriolar smooth muscle cells (25, 26). As with SDRT, TNF-α–induced vasoconstriction is annihilated by siRNA downregulation of endothelial *asmase* (54) and by the selective ET$_A$R antagonist BQ-123 (54).

Our data showing that endothelial apoptosis is dissociated from SDRT-I/R effects on DDR are consistent with recent studies reporting a parallel CRP engagement via NOX in the ER stress response to signal endothelial apoptosis (56). The apoptotic pathway manifests in HUVECs as NOX4-dependent activation of the ER stress sensors IRE1, PERK, and AFT6 (56), shown to signal apoptosis via JNK (57), a kinase employed by bovine aortic endothelial cells to signal apoptosis after SDRT (58). Whereas CRPs appear to initiate I/R vasoconstriction and apoptosis concurrently, dose dependencies for these biologies are indistinguishable. Nonetheless, 3 independent lines of evidence reported here support a shift in our understanding of SDRT tumor cure from endothelial apoptosis to I/R injury. Firstly, detailed kinetic studies of both responses indicate that SDRT-I/R is induced by 30 minutes, while the first evidence of apoptosis is detected at approximately 2 hours after SDRT (20). Second is the finding that clamping of tumors in *asmase*$^{-/-}$ mice after SDRT restores WT HDR loss of function and SDRT tumor cure, without apoptosis induction. Thirdly, differential abrogation of SDRT-I/R and HDR loss-of-function tumor cure by pretreatment with BQ-123 with no demonstrable effect on apoptosis provides definitive evidence supporting the SDRT-I/R model.

The contribution of HDR to irradiated cell viability, defined here as a critical target for SDRT tumor cure, has previously been challenged because mammalian cells genetically deficient in RAD51B, RAD52, and RAD54 exhibited only mild clonogenic survival phenotypes (59), and presumably only approximately 15% of radiation-induced DSBs appear to mandate HDR repair (60). Nonetheless, comparative elutriation experiments using RAD51D1-deficient and isogenic *CgRAD51D*-complemented RAD51D1.3 CHO cell lines show that HDR governs the late S-phase response, the most radioresistant phase of a cycling cell population, and that HDR loss in cycling RAD51D1-mutated cells radiosensitizes clonogenic lethality 2.8-fold (61). Furthermore, a set of normal-tissue and tumor stem cells engage HDR preferentially, or in some instances exclusively, in radiation-induced DSB repair. Specifically, *C. elegans* Notch-dependent germline cells, and the human Notch-driven adult CUTLL-1 stem cells of T cell lymphoblastic tumors, employ HDR exclusively for radiation-induced DSB repair (62), and downregulation of HDR, but not other DSB repair pathways, enhances radiation-induced germline

ablation and increases CUTLL-1 xenograft cure at 12 Gy from 33% to 83% (62). We also reported that mitotically active Wnt-driven small-intestinal Lgr5$^+$ crypt base columnar stem cells preferentially employ HDR to repair DSBs and are highly susceptible to DSB unrepair after potentially lethal high single-dose radiation exposure, associated with generation of numerous aberrant mitotic figures (63). Notably, a PARP/PolJ–mediated DSB repair mechanism can rescue cell survival after HDR inactivation via microhomology-mediated end joining (64, 65). However, this mechanism, if activated, would appear insufficient to save tumor cells after ultrahigh SDRT, as clinical evidence indicates higher than 90% tumor ablation with 24 Gy SDRT. As the populations considered critical to tumor cure, S-phase cells and tumor stem cells, display unique dependence on HDR to repair DSBs, we posit that HDR represents a point of tumor vulnerability accessed by SDRT biology, accounting for the unanticipated clinical success of SDRT.

The fundamental differences in mechanism of tumor ablation dictate how conventional fractionated radiotherapy and SDRT are delivered. While fractionated radiotherapy misrepair mandates multiple low-dose exposures to optimize therapeutic ratio, SDRT tumor cure via HDR loss of function mandates use of an ultrahigh radiation dose to generate an ASMase-mediated SSR sufficiently robust to deplete chromatin-bound SUMO3. At present, there are no technical differences in implementation of single versus fractionated radiotherapy, as the technological precision enabling SDRT has also revolutionized fractionated radiotherapy, allowing for safe delivery of daily doses exceeding 1.8–2.5 Gy per fraction, an approach termed hypofractionation. Hypofractionation involving 3–5 fractions of 5–10 Gy per fraction (66, 67), like classic fractionation, obeys principles of the linear quadratic model and is considered to employ the same 4R mechanism of tumor cure (68). However, the best clinical hypofractionation outcomes have been achieved with use of 3 treatment sessions of ultrahigh 14–20 Gy each (69), with outcomes of 3×18–20 Gy closely mimicking those realized with 24 Gy SDRT (70–72). Notably, at this ultrahigh dose range the linear quadratic model collapses, consistently underestimating tumor control by 20%–50% (73) by overpredicting iso-cure biologically effective doses (68), suggesting a biologic mechanism differing from gradual fractionated buildup of lethal misrepair. Consistent with the notion that each ultrahigh-dose hypofractionated exposure exceeds the threshold for activating the dual-target model described here, our ongoing preclinical mouse studies show that 3×15 Gy at 48-hour intervals, a protocol yielding approximately 50% durable control of human lung and liver metastasis (69), engages SDRT biology following each fraction (Bodo and Fuks, unpublished observations), indicating that ultrahigh-dose hypofractionation may functionally constitute a series of mini-SDRTs. Based on these considerations, the logic of using ultrahigh hypofractionation for tumor ablation should be reconsidered, as curative treatment mandates use of 3 mini-SDRT exposures associated with 3-fold increased risk of inadvertent machine or human error, and a higher cost.

The strategic approach to explore tumor cell DDR in its natural milieu of the anatomically unperturbed tumor in vivo yielded the discovery of the dynamic vascular dysfunction arm, and the surprising finding that the intensity of I/R regulates the level of radiation-induced clonogen lethality. While the DCE-MRI and

OxyLite data provide definitive evidence that deep hypoxia is mandatory for SDRT lethality, the level of pO_2 decrement required to maximize the SSR and chromatin free SUMO3 depletion, and whether there is a role for reperfusion in this response, remain unknown. Studies by Braun et al. (74) show that the OxyLite probe averages pO_2 within a large "measurement volume" of tissue that exceeds the diffusion range of oxygen from the capillary wall, with readouts tending to be strongly influenced by intravascular pO_2 (74). Hence, it is likely that our OxyLite data artificially underestimate the extent and severity of SDRT-induced interstitial tumor hypoxia. While precise quantitation of SDRT-I/R relative to SDRT tumor lethality remains to be established, evidence that its intensity determines the magnitude of SDRT-induced tumor cure is derived from our studies showing that exclusive adenoviral transduction of the *asmase* gene into dividing neo-angiogenic tumor endothelium to enhance ceramide-driven vascular dysregulation (16) enables a 25% reduction of the ablative SDRT dose normally required for tumor iso-cure at 20 Gy. As the number of DSBs per gray is constant across all mammalian cells and linear with dose (47), these data indicate that intensities of ASMase–I/R–ROS injury and resultant HDR loss of function, not number of DSB lesions per se, determine SDRT outcome, a paradigm that defies dogma in the field.

Consistent with this notion, early phase I dose escalation studies demonstrated a steep tumor dose-ablation curve for all tumor types between 18 Gy and 24 Gy SDRT, establishing 24 Gy as yielding more than 90% initial local tumor control (2, 3), consistent with 24 Gy being required to render sufficiently robust I/R-chromatin–bound SUMO3 depletion to promote ablation of all tumor types. The efficacy and limitations of 24 Gy SDRT have been addressed in a recent phase II clinical study of 566 oligometastatic lesions in 175 patients, validating that 24 Gy SDRT, when feasible, renders actuarial 92%–97% toxicity-free tumor ablation at 5 years, regardless of tumor size, type, or organ in which tumor was targeted (Greco and Fuks, unpublished observations). However, in 134 (24%) random lesions, application of 24 Gy SDRT was not possible because of tumor adherence to a critical normal organ, rendering unacceptable risk of severe normal-tissue toxicity. An established nontoxic state-of-the-art hypofractionated 3×9 Gy schedule was used in these instances, which yielded an actuarial 5-year tumor ablation in only 38% ($P < 0.0001$ vs. 24 Gy SDRT). An alternative to this schedule with proven ablative potential would be the use of ultrahigh-dose hypofractionated radiotherapy, shown to be subject to the same critical normal-tissue dose restrictions as 24 Gy SDRT (75). We thus posit that current radio-ablative technology is incapable of resolving this anatomical challenge, and that a biology-directed solution is required. The selective tumor versus normal-tissue radiosensitization enabled by adenoviral *asmase* transduction, or alternative pharmacologic approaches based on accessing tractable targets of SDRT/ASMase biology, currently under preclinical investigation (20, 76), provide a potential approach to de-escalate the SDRT ablative dose to below the threshold of normal-tissue toxicity. Translation of this approach into clinical use may afford conversion of intractable tumors to toxicity-free SDRT tumor cure, challenging surgery as the lead modality in curative human cancer ablation.

Methods

Supplemental Methods are available online with this article; https://doi.org/10.1172/JCI97631DS1.

Tumor diffusion/perfusion using Hoechst 33342. Diffusion/perfusion using the fluorescent dye Hoechst 33342 (*bis*-benzimide fluorochrome; Sigma-Aldrich, B2261) (15 mg/kg) was performed as described previously (21), measuring dye accumulation in tumor interstitial space at 2 minutes after i.v. injection. Intensity of dye fluorescence was determined in fresh-frozen 5-μm tumor sections using confocal microscopy (DM IRE2 inverted stand, Leica TCS SP2 AOBS laser confocal scanner; Memorial Sloan Kettering Cancer Center, Molecular Cytology Core Facility). Whole-mount sections were quantitatively analyzed using MetaMorph Software. Identified regions of necrosis were excluded from analysis. Pixel intensities in 8-bit images ranged from 0 to 255.

In vivo DCE-MRI. Dynamic contrast–enhanced ^1H MRI (DCE-MRI) was performed on a 7T magnetic resonance (MR) spectrometer using a home-built solenoidal ^1H MR coil. The animal was anesthetized with isoflurane mixed into 100% oxygen applied with a nose cone. Proton MR images were acquired using the Fast Low Angle Shot (FLASH) sequence with a 3.1-millisecond echo time (TE), 1 mm slice thickness (st), field of view (FOV) of (1.1 to 1.5) cm × (1.1 to 1.5) cm (depending on tumor size), 128 × 128 matrix, 45° flip angle, and 1 average. Anatomical ^1H MR images (16 slices, 134 milliseconds relaxation time [TR], 1 repetition) followed by spin density ^1H MR images (4 slices, 500 milliseconds TR, 1 repetition) were acquired to facilitate subsequent slice alignment of the postradiation MR images to the preirradiation MR images. T_1-weighted DCE-MRI (4 slices, 33 milliseconds TR, 312 repetitions) was performed at 4.3 seconds temporal resolution. The MR contrast agent Gd-DTPA (0.2 mM Gd/kg; Magnevist, Berlex Laboratories Inc.) was injected via the tail vein after 2 minutes of baseline acquisition followed by 20 minutes of dynamic acquisition. DCE-MRI images were obtained before irradiation, followed by recovery for at least 3 hours to ensure complete clearance of Gd-DTPA, with the tail vein catheter kept patent by injection of heparinized saline. Radiation-induced changes of tumor blood flow/perfusion were evaluated in a second DCE-MRI performed at 30 minutes after tumor irradiation. Experimental time-signal curves for each individual pixel in the MR images were normalized with respect to baseline signal (averaged over initial 2 minutes of acquisition without contrast agent) and fitted using the Hoffmann model (77) for each slice. An amplitude (A), which reflects degree of relative MR signal enhancement, and an exchange rate, which characterizes velocity of MR signal increase, can be obtained via pharmacokinetic modeling of the 2 compartments. Consequently, the Ak_{ep} value is analogous to the slope of MR signal enhancement and is considered an approximate measure of vascular flow/perfusion and permeability of tumor tissue (22). For pre- and postirradiation MRI, Ak_{ep} values of all 4 MR slices were combined into 1 histogram and median Ak_{ep} value calculated.

OxyLite oxymetry in vivo. Tumor and normal-tissue oxygen tension in situ was measured using the OxyLite 2000E oxymetry system (Oxford Optronics), which determines tissue oxygen tension using a fluorescence quenching technique (78). Briefly, OxyLite is an optical device that consists of a fiber optic probe, 220 μm in diameter, inserted into the core of the tumor via a 24-gauge removable needle, and a monitor that analyzes signals accrued by the probe to generate output tissue pO_2 data. The OxyLite approach to oxymetry is based on the principle that the presence of oxygen in tissue quenches light emitted by a flu-

orescent dye (ruthenium luminophore) impregnated at the probe tip. The lifetime of a ruthenium fluorescence pulse is inversely proportional to the oxygen tension in the surrounding tumor interstitial space, detected by a probe-assembled photomultiplier and translated into instantaneous pO_2 readout. Repeated ruthenium fluorescence pulses produced every 10–30 seconds enables robust assessment of pO_2 changes within tumor volume before, during, and after tumor exposure to SDRT. The mice were mildly anesthetized under isoflurane and placed throughout the experiment within the irradiator chamber with the fiber optic probe in place monitoring the same subvolume of the tumor tissue. Measurements were performed for 5 minutes before irradiation, to assure that the system was at equilibrium, and subsequently during radiation exposure and for 20–30 minutes thereafter.

IHC studies of DSB repair foci. Paraffin-embedded tissue sections (3 μm) were melted on a heat block, deparaffinized by 3 × 10 minutes in xylene, 2 × 3 minutes in 100% ethanol, 2 × 3 minutes in 95% ethanol, and 2 × 3 minutes in 70% ethanol, then washed with distilled water and transferred to 1× PBS. Antigen retrieval was performed in boiled 0.1-M citric acid buffer (pH 6.0) either in a steamer at 100°C for 30 minutes or in a Decloaking Chamber (Dako) at 125°C for 3–5 minutes, cooled for 20 minutes at room temperature, washed with distilled water, and transferred to washing buffer containing 0.1% Triton X-100 in 1× PBS. Foci were then probed using antibodies against established radiation-stimulated proteins overnight at 4°C. ProLong Gold and SlowFade Anti-fade reagent with DAPI (Vector Laboratories) were used to protect from photobleaching and quenching of fluorescent signal, respectively.

Antibodies used for IHC studies. Primary antibodies included γH2AX mouse monoclonal antibody against γH2AX-Ser139 (Millipore [clone JBW 301], 05-636; dilution 1:1,000), rabbit polyclonal anti-53BP1 (Novus Biologicals, NB100-304; dilution 1:1,000), rabbit polyclonal anti-BRCA1 (Ser 1387) (Novus Biologicals, NB100-225SS; dilution 1:250), mouse monoclonal anti-Rad51 (51RAD01) (Abcam, ab1837; dilution 1:50), mouse monoclonal anti–DNA-PKcs (phospho-T2609) (Abcam, ab18356; dilution 1:250), rabbit polyclonal anti-XRCC4 (Santa Cruz Biotechnology, sc-8285; dilution 1:50), mouse monoclonal anti-MDC1 (Millipore, 05-1572 [clone P2B11]; dilution 1:100), rabbit polyclonal anti-RAP80 (Novus Biologicals, NBP1-87156; dilution 1:50), rabbit polyclonal anti-RNF4 (gift from Jorma Palvimo, Institute of Biomedicine, University of Eastern Finland, Kuopio, Finland) (79), rabbit polyclonal anti-SUMO2/3 (Abcam, ab3742; dilution 1:100), mouse monoclonal anti-RPA2 (Abcam, ab2175; dilution 1:50), and anti-PIAS1 (Abcam, 32219; dilution 1:200). F(ab′)₂ goat anti-rabbit or anti-mouse IgG (H+L) cross-adsorbed secondary antibody conjugated to Alexa Fluor 488 (Thermo Fisher Scientific, A-11070 and A-11017; 2 mg/ml) was used at a dilution of 1:400.

Microscopy of DSB repair foci. Multichannel fluorescence images were acquired using an upright wide-field Zeiss Axio2 Imaging Microscope with AxioCam MRm Camera (1,360 × 1,036 pixels image array) and 40 × 2 objective of Zeiss Plan-Neofluar 1.3NA oil DIC (1083-997). Exposure time was set based on images of intermediate intensity, avoiding oversaturation from brightest foci. Once exposure time was set, it was kept constant within each set of experiments. Microscopy yielded blue DAPI staining of nuclear areas, fluorescent foci staining, or overlays of colocalized images. Twenty to 30 images containing 70–100 nuclei per image were randomly selected from each tissue section for quantitation of focus numbers. MetaMorph 7.6 software (Molecular Devices) was used for image analysis, adapted from pub-

lished studies (80). We used foci produced at low I/R dose (2 Gy at 30 minutes) to calibrate the system, measuring size and fluorescence intensity of individual foci, avoiding focus overlap. Two methods were used to quantify foci. Initially, manual focus counting was determined by eye. Faint foci considered below detection threshold were not quantified. Once mean size and fluorescence intensity per focus were determined, threshold for focus detection was tested manually, yielding 8.28 pixels as average focus size, consistent with published results (80). At the high radiation dose range, individual foci could not be distinguished until 3 hours after I/R, as nuclei were uniformly loaded with overlapping foci. Foci numbers at 30 minutes after high-dose I/R were estimated by measurement of mean fluorescence per nucleus, normalized to mean pixel focus intensity derived from 2-Gy data to estimate number of foci per nucleus, as published (80).

In vitro clonogenic assay. ShScramble, shSUMO2, and shSUMO3 cells were quantified by hemocytometer using trypan blue exclusion to assure viability. Cells were irradiated at 2–5 Gy in suspension and then plated in 10% FBS McCoy's 5A Medium at dilutions of 1,000–60,000 cells per plate, and after 10 days colonies (>50 cells) were fixed in 4% paraformaldehyde, stained with 0.1% crystal violet, and counted. Radiation dose–survival curves were analyzed and plotted as published (81).

Clinical IVIM DW-MRI. All patients underwent diffusion-weighted MRI (DW-MRI) before and after SDRT on a 3 Tesla MR scanner (MR750, GE Healthcare). Post-treatment DW-MRI acquisition began, on average, 26 minutes after completion of radiotherapy. IVIM DW-MRI was acquired at several consecutive time points with 4-minute intervals between acquisitions. A body coil was used for excitation. For signal reception, the vendor's standard 6-element spine phased-array coil was used, allowing simultaneous operation of 4 of the 6 array coils, and reconstruction of a sum-of-squares image from the 4 intermediate coil MR images. The MR imaging protocol enabled acquisition of multiple contiguous 2D slices in a fashion similar to functional MRI studies, multiple *b* values, data censorship, and offline averaging (82). This protocol enables acquisition of images with multiple *b* values dynamically in 1–4 series, and offers an option to vary the number of *b* values and the order of acquisition of different *b*-value MR images. DW images were obtained using a Stejskal-Tanner pulsed gradient spin echo sequence, containing 2 gradient pulses (duration δ), with start times separated by Δ, followed by a spin echo–echo planar imaging (SE-EPI) sequence. Dynamic multi–*b* value DW-MRI (b = 0, 10, 40, 70, 90, 100, 110, 120, 170, 210, 240, 270, 390, 530, 620, 750, 1,000 s/mm²) was acquired using the following parameters: TR/TE = 2,200/80.2 ms, 2 averages, matrix 128 × 128, FOV 320 × 160 mm², spatial resolution 2,5 × 1.25 × 5 mm³, with an acceleration factor of 2 and an acquisition time of about 2 minutes. Acquisition was repeated on average 16 times for a total of 32 minutes. Conventional T_1- and T_2-weighted MR images were also acquired for anatomical correlation using a standard-of-care clinical protocol. Perfusion fraction (*f*), pseudo-diffusion coefficient (*D**), and diffusion coefficient (*D*) were calculated for each lesion using a biexponential signal decay model and incorporating a correction to account for differences in the T_1 and T_2 relaxation times of tissue and blood, respectively. Volumes of interest covering irradiated lesions were outlined by experienced MRI radiologists on *D**, *D*, and *f* parametric maps, using a combination of the T_1-weighted and DW-MR images for guidance. Stability of the non-monoexponential model to data noise was confirmed by determination of the strength of cross-correlation among parameters and precision, and goodness of fit evaluated. For the IVIM

DW-MRI study, post-processing MRI was performed by a physicist using in-house software written in Matlab (MathWorks).

Statistics. Statistical analyses were performed using GraphPad Prism software (version 7). The unpaired 2-tailed *t* test was used, unless otherwise indicated, to calculate the *P* values. *$P < 0.05$, **$P < 0.01$, ***$P < 0.001$, ****$P < 0.0001$ were considered significant. For multiple comparisons, the Bonferroni correction was used. Ex vivo and in vitro clonogenic dose-survival curves were calculated by least-squares regression analysis, with a modification of the FIT software program as published (81). For tumor growth studies, Fisher's exact test was used to compare tumor cure events.

Study approval. Mice were housed at the animal housing facility of Memorial Sloan Kettering Cancer Center, a facility approved by the American Association for Assessment and Accreditation of Laboratory Animal Care, and maintained in accordance with the regulations and standards of the United States Department of Agriculture and the Department of Health and Human Services, NIH. Protocols for conducting animal experiments were approved by the Memorial Sloan Kettering Cancer Center Research Animal Resource Center. The prostate cancer IVIM DW-MRI data described in Figure 1F and Supplemental Table 1 were derived from the prospective randomized phase II study titled "Ultra-high-dose Hypofractionated vs. Single-dose Image-Guided Radiotherapy for Prostate Cancer (PROSINT)," approved by the Champalimaud Ethics Committee, and registered at ClinicalTrials.gov as NCT02570919; all patients signed an informed consent. The oligometastatic bone lesion IVIM DW-MRI data described in Figure 1G and Supplemental Table 2 were derived from the prospective randomized phase III study titled "Radiotherapy of oligometastatic bone lesions in patients undergoing IVIM DW-MRI," approved by the Memorial Sloan Kettering Cancer Center Institutional Review Board (10-154), and registered at ClinicalTrials.gov as NCT01223248; all patients signed an informed consent.

Author contributions

SB, CC, THT, AR, GH, and JDF performed experiments. SB and JDF maintained mouse colonies. SB, MGK, HJC, and EA performed tumor irradiation. DCE-MRI experiments were designed by JAK and EA. SB, EA, and HJC performed DCE-MRI experiments with assistance from MGK. DCE-MRI experiments were analyzed by EA and HJC. SB, HJH, and BE designed the oximetry experiments, which were performed by SB with assistance from JR. DSH and CG served as principal investigators of the clinical trials. JZ, CRC, SSR, YY, and MJZ recruited patents and gathered data for the clinical trials. DSH, YM, CG, HAV, and ES performed the IVIM DW-MRI studies. SB performed the Prdx6 overexpression experiments with assistance from SK. CCC provided pathology support. KMT provided microscopy support. ZZ supervised the statistical analysis. ZF, RK, SNP, ES, and AHF provided overall scientific direction and wrote the manuscript.

Address correspondence to: Richard Kolesnick, Memorial Sloan Kettering Cancer Center, 1275 York Avenue, New York, New York 10065, USA. Phone: 646.888.2172; Email: r-kolesnick@ski-mskcc.org.

CC's present address is: Technology Transfer Officer, Institut Curie, Paris, France.

THT's present address is: Biorepository and Pathology CoRE, Icahn School of Medicine at Mount Sinai, New York, New York, USA.

GH's present address is: Institute of Radiation Medicine, Fudan University, Shanghai, China.

HC's present address is: Biomedical Engineering and Medical Physics, Ulsan National Institute of Science and Technology, Ulsan, South Korea.

MGK's present address is: Department of Surgery, Penn State Hershey Medical Center, Hershey, Pennsylvania, USA.

ES's present address is: Department of Radiology and Cancer Research UK Cambridge Center, Cambridge Biomedical Campus, Cambridge, United Kingdom.

1. Leibel SA, Ling CC, Kutcher GJ, Mohan R, Cordon-Cordo C, Fuks Z. The biological basis for conformal three-dimensional radiation therapy. *Int J Radiat Oncol Biol Phys*. 1991;21(3):805–811.
2. Yamada Y, et al. High-dose, single-fraction image-guided intensity-modulated radiotherapy for metastatic spinal lesions. *Int J Radiat Oncol Biol Phys*. 2008;71(2):484–490.
3. Greco C, et al. Predictors of local control after single-dose stereotactic image-guided intensity-modulated radiotherapy for extracranial metastases. *Int J Radiat Oncol Biol Phys*. 2011;79(4):1151–1157.
4. Zelefsky MJ, et al. Tumor control outcomes after hypofractionated and single-dose stereotactic image-guided intensity-modulated radiotherapy for extracranial metastases from renal cell carcinoma. *Int J Radiat Oncol Biol Phys*. 2012;82(5):1744–1748.
5. Yamada Y, et al. The impact of histology and delivered dose on local control of spinal metastases treated with stereotactic radiosurgery. *Neurosurg Focus*. 2017;42(1):E6.
6. Foray N, Arlett CF, Malaise EP. Radiation-induced DNA double-strand breaks and the radiosensitivity of human cells: a closer look. *Biochimie*. 1997;79(9-10):567–575.

7. Jackson SP, Bartek J. The DNA-damage response in human biology and disease. *Nature*. 2009;461(7267):1071–1078.

8. Withers HR. Failla memorial lecture. Contrarian concepts in the progress of radiotherapy. *Radiat Res*. 1989;119(3):395–412.

9. Rothkamm K, Löbrich M. Misrepair of radiation-induced DNA double-strand breaks and its relevance for tumorigenesis and cancer treatment (review). *Int J Oncol*. 2002;21(2):433–440.

10. Huang L, Snyder AR, Morgan WF. Radiation-induced genomic instability and its implications for radiation carcinogenesis. *Oncogene*. 2003;22(37):5848–5854.

11. Iliakis G, Murmann T, Soni A. Alternative end-joining repair pathways are the ultimate backup for abrogated classical non-homologous end-joining and homologous recombination repair: implications for the formation of chromosome translocations. *Mutat Res Genet Toxicol Environ Mutagen*. 2015;793:166–175.

12. Budach W, Taghian A, Freeman J, Gioioso D, Suit HD. Impact of stromal sensitivity on radiation response of tumors. *J Natl Cancer Inst*. 1993;85(12):988–993.

13. Okunieff P, Morgan D, Niemierko A, Suit HD. Radiation dose-response of human tumors. *Int J Radiat Oncol Biol Phys*. 1995;32(4):1227–1237.

14. Garcia-Barros M, et al. Tumor response to radiotherapy regulated by endothelial cell apoptosis. *Science*. 2003;300(5622):1155–1159.

15. García-Barros M, et al. Impact of stromal sensitivity on radiation response of tumors implanted in SCID hosts revisited. *Cancer Res*. 2010;70(20):8179–8186.

16. Stancevic B, et al. Adenoviral transduction of human acid sphingomyelinase into neoangiogenic endothelium radiosensitizes tumor cure. *PLoS One*. 2013;8(8):e69025.

17. Fuks Z, Kolesnick R. Engaging the vascular component of the tumor response. *Cancer Cell*. 2005;8(2):89–91.

18. Lewicki MC, Srikumar T, Johnson E, Raught B. The S. cerevisiae SUMO stress response is a conjugation-deconjugation cycle that targets the transcription machinery. *J Proteomics*. 2015;118:39–48.

19. Enserink JM. Sumo and the cellular stress response. *Cell Div*. 2015;10:(4):doi:10.1186/s13008-015-0010-1.

20. Truman JP, et al. Endothelial membrane remodeling is obligate for anti-angiogenic radiosensitization during tumor radiosurgery. *PLoS One*. 2010;5(8):e12310.

21. Li XF, Carlin S, Urano M, Russell J, Ling CC, O'Donoghue JA. Visualization of hypoxia in microscopic tumors by immunofluorescent microscopy. *Cancer Res*. 2007;67(16):7646–7653.

22. Cho H, et al. Noninvasive multimodality imaging of the tumor microenvironment: registered dynamic magnetic resonance imaging and positron emission tomography studies of a preclinical tumor model of tumor hypoxia. *Neoplasia*. 2009;11(3):247–259.

23. Griffiths JR, Robinson SP. The OxyLite: a fibre-optic oxygen sensor. *Br J Radiol*. 1999;72(859):627–630.

24. Dewhirst MW. Relationships between cycling hypoxia, HIF-1, angiogenesis and oxidative stress. *Radiat Res*. 2009;172(6):653–665.

25. Ihara M, et al. In vitro biological profile of a highly potent novel endothelin (ET) antagonist BQ-123 selective for the ETA receptor. *J Cardiovasc Pharmacol*. 1992;20(suppl 12):S11–S14.

26. Pernow J, Wang QD. Endothelin in myocardial ischaemia and reperfusion. *Cardiovasc Res*. 1997;33(3):518–526.

27. Le Bihan D, Turner R. The capillary network: a link between IVIM and classical perfusion. *Magn Reson Med*. 1992;27(1):171–178.

28. Löbrich M, et al. γH2AX foci analysis for monitoring DNA double-strand break repair: strengths, limitations and optimization. *Cell Cycle*. 2010;9(4):662–669.

29. Halestrap AP, Clarke SJ, Khaliulin I. The role of mitochondria in protection of the heart by preconditioning. *Biochim Biophys Acta*. 2007;1767(8):1007–1031.

30. Brown JM. Tumor microenvironment and the response to anticancer therapy. *Cancer Biol Ther*. 2002;1(5):453–458.

31. Panier S, Boulton SJ. Double-strand break repair: 53BP1 comes into focus. *Nat Rev Mol Cell Biol*. 2014;15(1):7–18.

32. Jackson SP, Durocher D. Regulation of DNA damage responses by ubiquitin and SUMO. *Mol Cell*. 2013;49(5):795–807.

33. Luo K, Zhang H, Wang L, Yuan J, Lou Z. Sumoylation of MDC1 is important for proper DNA damage response. *EMBO J*. 2012;31(13):3008–3019.

34. Psakhye I, Jentsch S. Protein group modification and synergy in the SUMO pathway as exemplified in DNA repair. *Cell*. 2012;151(4):807–820.

35. Waypa GB, Smith KA, Schumacker PT. O2 sensing, mitochondria and ROS signaling: the fog is lifting. *Mol Aspects Med*. 2016;47-48:76–89.

36. Yang W, Sheng H, Warner DS, Paschen W. Transient global cerebral ischemia induces a massive increase in protein sumoylation. *J Cereb Blood Flow Metab*. 2008;28(2):269–279.

37. Tatham MH, et al. Polymeric chains of SUMO-2 and SUMO-3 are conjugated to protein substrates by SAE1/SAE2 and Ubc9. *J Biol Chem*. 2001;276(38):35368–35374.

38. Datta S, Snow CJ, Paschal BM. A pathway linking oxidative stress and the Ran GTPase system in progeria. *Mol Biol Cell*. 2014;25(8):1202–1215.

39. Kodiha M, Chu A, Matusiewicz N, Stochaj U. Multiple mechanisms promote the inhibition of classical nuclear import upon exposure to severe oxidative stress. *Cell Death Differ*. 2004;11(8):862–874.

40. Guzy RD, Schumacker PT. Oxygen sensing by mitochondria at complex III: the paradox of increased reactive oxygen species during hypoxia. *Exp Physiol*. 2006;91(5):807–819.

41. Fisher AB. Peroxiredoxin 6 in the repair of peroxidized cell membranes and cell signaling. *Arch Biochem Biophys*. 2017;617:68–83.

42. Wilcox CS. Effects of tempol and redox-cycling nitroxides in models of oxidative stress. *Pharmacol Ther*. 2010;126(2):119–145.

43. Rhee SG, Kil IS. Multiple functions and regulation of mammalian peroxiredoxins. *Annu Rev Biochem*. 2017;86:749–775.

44. Bucana C, Saiki I, Nayar R. Uptake and accumulation of the vital dye hydroethidine in neoplastic cells. *J Histochem Cytochem*. 1986;34(9):1109–1115.

45. Fenech M, Morley AA. Measurement of micronuclei in lymphocytes. *Mutat Res*. 1985;147(1–2):29–36.

46. Proia NK, Paszkiewicz GM, Nasca MA, Franke GE, Pauly JL. Smoking and smokeless tobacco-associated human buccal cell mutations and their association with oral cancer — a review. *Cancer Epidemiol Biomarkers Prev*. 2006;15(6):1061–1077.

47. Ward JF. The yield of DNA double-strand breaks produced intracellularly by ionizing radiation: a review. *Int J Radiat Biol*. 1990;57(6):1141–1150.

48. Fu C, et al. Stabilization of PML nuclear localization by conjugation and oligomerization of SUMO-3. *Oncogene*. 2005;24(35):5401–5413.

49. Wang L, Wansleeben C, Zhao S, Miao P, Paschen W, Yang W. SUMO2 is essential while SUMO3 is dispensable for mouse embryonic development. *EMBO Rep*. 2014;15(8):878–885.

50. Gulbins E, Kolesnick R. Raft ceramide in molecular medicine. *Oncogene*. 2003;22(45):7070–7077.

51. Cremesti A, et al. Ceramide enables fas to cap and kill. *J Biol Chem*. 2001;276(26):23954–23961.

52. Grassme H, et al. CD95 signaling via ceramide-rich membrane rafts. *J Biol Chem*. 2001;276(23):20589–20596.

53. Stancevic B, Kolesnick R. Ceramide-rich platforms in transmembrane signaling. *FEBS Lett*. 2010;584(9):1728–1740.

54. Li PL, Zhang Y, Yi F. Lipid raft redox signaling platforms in endothelial dysfunction. *Antioxid Redox Signal*. 2007;9(9):1457–1470.

55. Alonso D, Radomski MW. The nitric oxide-endothelin-1 connection. *Heart Fail Rev*. 2003;8(1):107–115.

56. Galán M, Kassan M, Kadowitz PJ, Trebak M, Belmadani S, Matrougui K. Mechanism of endoplasmic reticulum stress-induced vascular endothelial dysfunction. *Biochim Biophys Acta*. 2014;1843(6):1063–1075.

57. Hong D, et al. Ox-LDL induces endothelial cell apoptosis via the LOX-1-dependent endoplasmic reticulum stress pathway. *Atherosclerosis*. 2014;235(2):310–317.

58. Verheij M, et al. Requirement for ceramide-initiated SAPK/JNK signalling in stress-induced apoptosis. *Nature*. 1996;380(6569):75–79.

59. Wang H, et al. Efficient rejoining of radiation-induced DNA double-strand breaks in vertebrate cells deficient in genes of the RAD52 epistasis group. *Oncogene*. 2001;20(18):2212–2224.

60. Beucher A, et al. ATM and Artemis promote homologous recombination of radiation-induced DNA double-strand breaks in G2. *EMBO J*. 2009;28(21):3413–3427.

61. Wilson PF, Hinz JM, Urbin SS, Nham PB, Thompson LH. Influence of homologous recombinational repair on cell survival and chromosomal aberration induction during the cell cycle in gamma-irradiated CHO cells. *DNA Repair (Amst)*. 2010;9(7):737–744.

62. Deng X, et al. Targeting homologous recombination in notch-driven C. elegans stem cell and human tumors. *PLoS One*. 2015;10(6):e0127862.

63. Hua G, et al. Distinct levels of radioresistance in Lgr5+ colonic epithelial stem cells versus Lgr5+ small intestinal stem cells. *Cancer Res*. 2017;77(8):2124–2133.

64. Ceccaldi R, et al. Homologous-recombination-deficient tumours are dependent on Polθ-mediated repair. *Nature*. 2015;518(7538):258–262.

65. Mateos-Gomez PA, Gong F, Nair N, Miller KM, Lazzerini-Denchi E, Sfeir A. Mammalian polymerase θ promotes alternative NHEJ and suppresses recombination. *Nature*. 2015;518(7538):254–257.

66. Salama JK, et al. Stereotactic body radiotherapy for multisite extracranial oligometastases: final report of a dose escalation trial in patients with 1 to 5 sites of metastatic disease. *Cancer*. 2012;118(11):2962–2970.

67. Aitken K, et al. Initial UK experience of stereotactic body radiotherapy for extracranial oligometastases: can we change the therapeutic paradigm? *Clin Oncol (R Coll Radiol)*. 2015;27(7):411–419.

68. Brown JM, Carlson DJ, Brenner DJ. The tumor radiobiology of SRS and SBRT: are more than the 5 Rs involved? *Int J Radiat Oncol Biol Phys*. 2014;88(2):254–262.

69. McCammon R, Schefter TE, Gaspar LE, Zaemisch R, Gravdahl D, Kavanagh B. Observation of a dose-control relationship for lung and liver tumors after stereotactic body radiation therapy. *Int J Radiat Oncol Biol Phys*. 2009;73(1):112–118.

70. Rusthoven KE, et al. Multi-institutional phase I/II trial of stereotactic body radiation therapy for lung metastases. *J Clin Oncol*. 2009;27(10):1579–1584.

71. Rusthoven KE, et al. Multi-institutional phase I/II trial of stereotactic body radiation therapy for liver metastases. *J Clin Oncol*. 2009;27(10):1572–1578.

72. Folkert MR, Timmerman RD. Stereotactic ablative body radiosurgery (SABR) or stereotactic body radiation therapy (SBRT). *Adv Drug Deliv Rev*. 2017;109:3–14.

73. Guerrero M, Li XA. Extending the linear-quadratic model for large fraction doses pertinent to stereotactic radiotherapy. *Phys Med Biol*. 2004;49(20):4825–4835.

74. Braun RD, Lanzen JL, Snyder SA, Dewhirst MW. Comparison of tumor and normal tissue oxygen tension measurements using OxyLite or microelectrodes in rodents. *Am J Physiol Heart Circ Physiol*. 2001;280(6):H2533–H2544.

75. Benedict SH, et al. Stereotactic body radiation therapy: the report of AAPM Task Group 101. *Med Phys*. 2010;37(8):4078–4101.

76. Rao SS, et al. Axitinib sensitization of high single dose radiotherapy. *Radiother Oncol*. 2014;111(1):88–93.

77. Hoffmann U, Brix G, Knopp MV, Hess T, Lorenz WJ. Pharmacokinetic mapping of the breast: a new method for dynamic MR mammography. *Magn Reson Med*. 1995;33(4):506–514.

78. Young WK, Vojnovic B, Wardman P. Measurement of oxygen tension in tumours by time-resolved fluorescence. *Br J Cancer Suppl*. 1996;27:S256–S259.

79. Häkli M, Karvonen U, Jänne OA, Palvimo JJ. SUMO-1 promotes association of SNURF (RNF4) with PML nuclear bodies. *Exp Cell Res*. 2005;304(1):224–233.

80. Böcker W, Iliakis G. Computational methods for analysis of foci: validation for radiation-induced γ-H2AX foci in human cells. *Radiat Res*. 2006;165(1):113–124.

81. Albright N. Computer programs for the analysis of cellular survival data. *Radiat Res*. 1987;112(2):331–340.

82. Mazaheri Y, Do RK, Shukla-Dave A, Deasy JO, Lu Y, Akin O. Motion correction of multi-b-value diffusion-weighted imaging in the liver. *Acad Radiol*. 2012;19(12):1573–1580.